2D Layered Perovskites

Solution Processable Materials

The recent discovery that single-layer 2D perovskites can be prepared using solution processing techniques[1] has been followed by enormous research into optoelectronic applications of 2D perovskites including light emitting diodes (LEDs),[2] phototransistors,[3] and solar cells.[4]

Tunable Emission Wavelength

Photoluminescent 2D perovskites have an emission wavelength that changes depending on the layer thickness and the choice of amine and halide. We offer an excellent portfolio of the most popular 2D perovskite compositions for photoluminescence based devices.

Improved Moisture Stability

Solar cells fabricated with 2D perovskites have improved stability in moist air compared to 3D perovskites.[4]

Formula	Cat. No.	Layer Thickness	$(RNH_3)_2(MeNH_3)_{n-1}Pb_nX_{3n+1}$		
			R	X	n
$(BA)_2PbI_4$	**910961**	n=1	Bu	I	1
$(BA)_2PbBr_4$	**910953**	n=1	Bu	Br	1
$(PEA)_2PbI_4$	**910937**	n=1	PE	I	1
$(PEA)_2PbBr_4$	**910945**	n=1	PE	Br	1
$(BA)_2(MA)Pb_2I_7$	**912816**	n=2	Bu	I	2
$(BA)_2(MA)_2Pb_3I_{10}$	**912557**	n=3	Bu	I	3
$(BA)_2(MA)_3Pb_4I_{13}$	**914363**	n=4	Bu	I	4
$(BA)_2(MA)_4Pb_5I_{16}$	**912301**	n=5	Bu	I	5

BA = n-butylammonium; PEA = 2-phenylethylammonium;
MA =methylammonium, Bu=n-butyl, PE=2-phenylethyl

References:

1) Dou, L.; Wong, A. B.; Yu, Y.; Lai, M.; Kornienko, N.; Eaton, S. W.; Fu, A.; Bischak, C. G.; Ma, J.; Ding, T.; Ginsberg, N. S.; Wang, L-W.; Alivisatos, A. P.; Yang, P. *Science* **2015,** *349,* 1518. DOI: 10.1126/science.aac7660
2) Yuan, M.; Quan, L. N.; Comin, R.; Walters, G.; Sabatini, R.; Voznyy, O.; Hoogland, S.; Zhao, Y.; Beauregard,E. M.; Kanjanaboos, P.; Lu, Z.; Kim, D. H.; Sargent, E. H. *Nat. Nanotechnol.* **2016,** *11,* 872. DOI: 10.1038/NNANO.2016.110
3) Shao, Y.; Liu, Y.; Chen, X.; Chen, C.; Sarpkaya, I.; Chen, Z.; Fang, Y.; Kong, J.; Watanabe, K.;Taniguchi, T.; Taylor, A.; Huang, J.; Xia, F. *Nano Lett.* **2017,** *17,* 7330. DOI: 10.1021/acs.nanolett.7b02980
4) Cao, D. H.; Stoumpos, C. C.; Farha, O. K.; Hupp, J. T.; Kanatzidis, M. G. *J. Am. Chem.* Soc. **2015,** *137,* 7843. DOI: 10.1021/jacs.5b03796

SigmaAldrich.com/perovskite

MK_AD9822EN 43729 09/2022

The Life Science business of Merck operates as MilliporeSigma in the U.S. and Canada.

Sigma-Aldrich®
Lab & Production Materials

ADVANCED ENERGY MATERIALS
www.advenergymat.de

Solution Processable Direct Bandgap Copper-Silver-Bismuth Iodide Photovoltaics: Compositional Control of Dimensionality and Optoelectronic Properties

Narendra Pai, Manjunath Chatti, Sebastian O. Fürer, Andrew D. Scully, Sonia R. Raga, Nitish Rai, Boer Tan, Anthony S. R. Chesman, Zhou Xu, Kevin J. Rietwyk, Saripally Sudhaker Reddy, Yvonne Hora, Gaveshana A. Sepalage, Nadja Glück, Monica Lira-Cantú, Udo Bach, and Alexandr N. Simonov**

The search for lead-free alternatives to lead-halide perovskite photovoltaic materials resulted in the discovery of copper(I)-silver(I)-bismuth(III) halides exhibiting promising properties for optoelectronic applications. The present work demonstrates a solution-based synthesis of uniform Cu_xAgBiI_{4+x} thin films and scrutinizes the effects of x on the phase composition, dimensionality, optoelectronic properties, and photovoltaic performance. Formation of pure 3D $CuAgBiI_5$ at $x = 1$, 2D Cu_2AgBiI_6 at $x = 2$, and a mix of the two at $1 < x < 2$ is demonstrated. Despite lower structural dimensionality, Cu_2AgBiI_6 has broader optical absorption with a direct bandgap of 1.89 ± 0.05 eV, a valence band level at -5.25 eV, improved carrier lifetime, and higher recombination resistance as compared to $CuAgBiI_5$. These differences are mirrored in the power conversion efficiencies of the $CuAgBiI_5$ and Cu_2AgBiI_6 solar cells under 1 sun of 1.01 ± 0.06% and 2.39 ± 0.05%, respectively. The latter value is the highest reported for this class of materials owing to the favorable film morphology provided by the hot-casting method. Future performance improvements might emerge from the optimization of the Cu_2AgBiI_6 layer thickness to match the carrier diffusion length of ≈40–50 nm. Nonencapsulated Cu_2AgBiI_6 solar cells display storage stability over 240 days.

1. Introduction

Solar energy conversion technologies already produce 4% of electricity worldwide, and this contribution will continue to proliferate to support our transition toward sustainable energy. This progress builds upon developments of new photovoltaic devices, like lead-halide perovskite solar cells, that have piqued strong interest from both industry and academia as a competitive alternative to the crystalline silicon technology that currently dominates the market. However, challenges in demonstrating the sufficient long-term stability of perovskite solar cells in operation and toxicity of Pb^{2+} are yet to be solved, which motivates the search for similarly effective but more stable and lead-free light harvesters.[1]

While the research on the homovalent substitution of lead(II) with cations like Sn^{2+} and Ge^{2+} in the perovskite structure

N. Pai, S. O. Fürer, N. Rai, B. Tan, K. J. Rietwyk, S. S. Reddy, Y. Hora, G. A. Sepalage, N. Glück, U. Bach
Department of Chemical Engineering
Monash University
Clayton, Victoria 3800, Australia
E-mail: udo.bach@monash.edu
N. Pai, S. S. Reddy, N. Glück, U. Bach
The Australian Centre for Advanced Photovoltaics (ACAP)
Monash University
Clayton, VIC 3800, Australia

The ORCID identification number(s) for the author(s) of this article can be found under https://doi.org/10.1002/aenm.202201482.

DOI: 10.1002/aenm.202201482

N. Pai, S. O. Fürer, K. J. Rietwyk, U. Bach
ARC Centre of Excellence for Exciton Science
Monash University
Clayton, Victoria 3800, Australia
M. Chatti, A. N. Simonov
School of Chemistry
Monash University
Clayton, Victoria 3800, Australia
E-mail: alexandr.simonov@monash.edu
A. D. Scully, A. S. R. Chesman
CSIRO Manufacturing
Clayton, Victoria 3168, Australia
S. R. Raga, M. Lira-Cantú
Institut Català de Nanociència i Nanotecnologia
Universitat Autònoma de Barcelona
Bellaterra, Barcelona 08193, Spain
Z. Xu
Monash Centre for Electron Microscopy
Monash University
Clayton, VIC 3800, Australia

is making outstanding progress in power conversion efficiency (PCE) terms, the resulting compounds are even less stable than their Pb-based counterparts.[2] In contrast, heterovalent metal substitution produces materials with excellent stability, yet their optoelectronic properties are significantly less favorable for photovoltaic applications.[3] For example, relatively stable bismuth(III)-based compounds with a generic formula $A_3Bi_2X_9$ (where $A^+ = CH_3NH_3^+$ or Cs^+, and $X^- = Cl^-$, Br^- or I^-) exhibit lower structural dimensionality with wide bandgaps ($E_g > 2$ eV) and higher excitonic binding energies (over 0.1 eV) as compared to lead(II) perovskites based on the same A^+ and X^- components, and therefore struggle to demonstrate high photovoltaic performance.[4]

Aiming to address this, research on replacing alkaline-earth A^+ cations with coinage metal cations, viz. Cu^+ and Ag^+, has demonstrated a structurally and electronically 3D $A_aB_bX_{a+3b}$ ($A = Cu^+$ or Ag^+; $B = Sb^{3+}$ or Bi^{3+}; $X = Cl^-$, Br^- or I^-) family of pnictogen halides with direct band transitions that outperform conventional bismuth iodide perovskites.[5] Although the relatively wide bandgaps of such compounds ($E_g > 1.85$ eV) were initially a limitation, bandgap engineering strategies have been introduced to produce better-performing photovoltaic devices. As a result, almost a fivefold increase in the PCE from ≈1.2 to 5.5% for solar cells based on silver bismuth iodides has been achieved within only a few years of research.[5a,b,6] However, Kulkarni et al. have demonstrated recently that the Ag^+ ion migration induces device degradation in the highest-performing silver-rich $Ag_aBi_bI_{a+3b}$ ($a > b$) compositions.[7] Replacing Ag^+ with Cu^+ was suggested to reduce the ion migration and associated issues, but introduced new problems, including phase instability. As a result, the overall progress in the photovoltaic performance improvements has been significantly slower for the copper-based compounds of this class (best PCE < 1.2 % reported so far).[6b,8]

Concurrently, computational studies by Savory et al. and Cai et al. revealed that replacing two adjacent Pb^{2+} with monovalent and trivalent cations could produce 2 × 2 × 2 supercell perovskites with a generic $A_2M^{1+}M^{3+}X_6$ formula, broadening opportunities for the design of new photovoltaic materials.[9] Among this family of compounds, $Cs_2AgBiBr_6$ received specific attention due to its high stability and a range of advantageous properties like small carrier effective mass (< $0.5m_0$), moderate charge carrier mobility (1 $cm^2\ V^{-1}\ s^{-1}$), and long carrier lifetime.[10] The latter parameter reported for $Cs_2AgBiBr_6$ single-crystals exceeds 1 µs, which theoretically corresponds to a very long carrier diffusion length over 1 µm (calculated using the carrier mobility value noted above). However, this material also presents a broad range of limitations, including an indirect wide bandgap (>2 eV), downshifted valence band edge (below −5.6 eV; hereinafter vs vacuum), shallow absorption edge with Urbach energy of 0.07 eV, and high trap-state density mediating charge-carrier trapping and nonradiative recombination.[11] Moreover, Snaith and co-workers reported that the $Cs_2AgBiBr_6$ thin-films exhibit very short, trap-restricted carrier lifetimes below 100 ns, which result in short electron and hole carrier diffusion lengths (≤30 and ≈150 nm, respectively).[12] As a result, $Cs_2AgBiBr_6$-based solar cells do not operate efficiently in the visible and infrared regions and have failed to produce short-circuit current densities above 6 mA cm^{-2} under 1 sun irradiation.[12,13] Attempts to improve the properties of $Cs_2AgBiBr_6$ by applying extreme pressures[14] and ionic substitution[15] produced some positive results, including a decrease in E_g and an increase in visible light absorption. However, it has proven challenging to translate these improvements to operational photovoltaic devices.[16] Even when the solar cells based on modified $Cs_2AgBiBr_6$ could be produced, the reported improvements did not enable PCEs at the level comparable to that of lower-dimensional bismuth perovskites.[16a,c] Moreover, none of the reported M-site modification strategies resulted in a strong direct bandgap transition predicted by theoretical studies.[9b,17]

Many of the performance-limiting band-structure problems of $Cs_2AgBiBr_6$ stem from the influence of Br p-orbitals on the valence band maxima (VBM) and conduction band maxima (CBM)[16d] and are therefore expected to be resolved upon transition to the iodide counterpart, viz. Cs_2AgBiI_6. Another constraint that needs to be resolved is the lower electronic dimensionality of $Cs_2AgBiBr_6$, which arises due to the isolation of the [$AgBr_6$] octahedra by the adjacent [$BiBr_6$] octahedra and results in the inability to connect VBM (contributed by Ag 4d and Br 5p orbitals) and CBM (contributed by Bi 6p orbitals) in three dimensions.[10] The iodide-based double perovskites were predicted to be devoid of these problems and to exhibit a direct band transition with improved dimensionality,[18] but Cs_2AgBiI_6 is, unfortunately, thermodynamically unstable[19] and decomposes into a lower-dimensional $Cs_3Bi_2I_9$.[20] Thus, no success has been achieved in synthesizing Cs_2AgBiI_6 so far, except in the form of a colloidal nanocrystal dispersion in toluene.[21]

A possible strategy to avoid phase decomposition of Cs_2AgBiI_6 is to replace large Cs^+ (174 pm) with cations that have smaller ionic radii.[22] While this approach did not produce positive results when using monovalent cations neighboring cesium, viz. Rb^+ (156 pm) or K^+ (146 pm), the substitution of Cs^+ with Cu^+ resulted in a stable Cu_2AgBiI_6 compound.[23] Unlike corner-shared lead-halide perovskites, Cu_2AgBiI_6 was reported to exhibit structural similarities with the edge-shared $A_aBi_bI_{a+3b}$ ($A = Cu^+$ or Ag^+) materials. When exploring the CuI-BiI_3 system, Sansom et al.[24] observed a metastable behavior of $CuBiI_4$, which decomposed back to CuI and BiI_3 under ambient conditions even without any irradiation. However, once AgI was introduced, a stable phase of Cu_2AgBiI_6 was formed and found to have a trigonal unit cell of space group $R3m$ forming a $CdCl_2$-type rhombohedral layered structure. It was also postulated that the introduction of Cu^+ reduces Ag^+ ion migration.[25] Thin films of the Cu_2AgBiI_6 material showed promising optoelectronic properties, including an absorption coefficient over 1×10^5 cm^{-1} within a 375–600 nm wavelength range, an exciton binding energy of 0.025 eV and a direct bandgap. Although the E_g value of 2.06 eV was still relatively high, it was also improved compared to ≈2.3 eV for $Cs_2AgBiBr_6$. However, a proof-of-concept Cu_2AgBiI_6-based solar cell delivered a low PCE of ≈0.4%, emphasizing the need for further research toward understanding the effects of the active layer morphology and composition along with the device architecture on the photovoltaic performance.[23]

Further exploration of the CuI-AgI-BiI_3 system by Sansom et al. revealed a 3D spinel $CuAgBiI_5$ composition, which is structurally close to spinel $CuBiI_4$ and Bi-rich $Ag_aBi_bI_{a+3b}$ ($a < b$) compounds. It was reported that the large trigonal unit cell with a 3D spinel octahedral motif had no significant effects on the optoelectronic capabilities of Cu_2AgBiI_6 compared to $CuAgBiI_5$.

This is distinct to the dimensional confinement effects observed in lead-halide and heterovalent lead-free perovskites.[24,26]

Overall, our current fundamental understanding of the correlations between dimensionality, structure, composition, and optoelectronic properties of the promising Cu-Ag-Bi-I materials is far from complete. Moreover, no photovoltaic devices based on $CuAgBiI_5$ have been reported yet, while those based on Cu_2AgBiI_6 delivered only low power conversion efficiencies below 1%.[27] Addressing this, we present herein a study of the compositional tunability of optoelectronic characteristics and associated photovoltaic performance for the Cu_xAgBiI_{4+x} system. One feature of the present work is the first demonstration of a solvent-based hot-casting method to prepare thin Cu_xAgBiI_{4+x} films with improved morphology and surface coverage, which allowed us to achieve the highest photovoltaic performance for these materials reported so far. Stability under ambient storage conditions on a timescale of months is also presented.

2. Results and Discussion

All materials investigated herein were synthesized by casting their precursor solutions in mixed dimethylsulfoxide (DMSO) + dimethylformamide (DMF) solvent system onto a substrate of interest, following the procedure summarized in Figure S1 (Supporting Information). Using this solvent-based synthesis strategy to produce M_cAgBiI_{4+c} materials with $M = Rb^+$ and K^+ was unsuccessful and resulted in phase segregation (Figure S2, Supporting Information). These results are consistent with previous reports.[24]

At the same time, the solvent-based procedure introduced herein was found to be effective for the fabrication of the Cu_xAgBiI_{4+x} films from the solutions containing equimolar concentrations of bismuth(III) and silver(I) iodides along with different amounts of copper(I) iodide. To overcome the solubility limitations of AgI and CuI in DMSO + DMF, the precursor solutions were heated to 80 °C and stirred for one hour, cooled down to ambient temperature, and filtered before deposition. The resulting homogenous red-colored solutions were spin-coated utilizing gas-assisted, anti-solvent, and hot-casting strategies. Films were deposited onto fluorine-doped tin(IV) oxide (FTO) coated glass modified with a compact titania layer (c-TiO_2; ≈15 nm thickness) and then with a mesoporous TiO_2 framework (m-TiO_2; ≈140 nm thickness; 30 nm average particle size), except for the glass-supported samples for the X-ray diffraction (XRD) and photoluminescence spectroscopic (PL) analysis. The experimental section provides further details on the preparation and characterization procedures.

2.1. Film Morphology, Composition, and Dimensionality

The use of conventional deposition methods, either with the gas flowing or different antisolvents applied to the spin-coated solution, produced heterogeneous coatings with a high concentration of pin-holes (Figure S3, Supporting Information), which could not be improved by adjusting the precursor concentrations and the DMSO:DMF ratio. To resolve this, we employed a temperature-assisted hot-casting strategy with the solutions and substrates preheated at different temperatures within a 60–120 °C range for 5 min and then immediately used for spin-coating. This method avoids the use of antisolvents and facilitates control over crystallinity, morphology, and composition of the produced coatings. Scanning electron microscopic (SEM) analysis showed that the best quality films with a minimal concentration of pin-holes and impurities are obtained with 0.45 M [Cu_xAgBiI_{4+x}] precursor concentration and a DMSO:DMF ratio of 3:1 vol (Figure S4, Supporting Information).

To further improve the quality of the films, which is critical for optoelectronic applications, the temperatures of the solution and substrate were optimized (Figure S5, Supporting Information). As determined by SEM, the best results were obtained with the solution and the mTiO_2|cTiO_2|FTO support both preheated to 100 °C (Figure S5, Supporting Information). Preheating controls the rate of crystallization and facilitates complete removal of DMSO from the films, i.e. avoids trapping of the solvent with a high boiling point (189 °C), which can induce the formation of pin-holes during postannealing. The latter was undertaken herein in two steps, viz. 80 °C followed by 150 °C to slow down the crystallization and minimize the loss of volatile iodide. The optimized hot-casting assisted spin-coating approach produces dark shiny films with visually uniform substrate coverage (Figure S6, Supporting Information). When formed, the investigated materials exhibit high thermal stability with the decomposition temperature above 250 °C (Figure S7, Supporting Information).

Another advantage of the hot-casting method is homogeneous nucleation of the target material throughout the support provided by preheating the latter, in contrast to conventional antisolvent- and gas-assisted strategies that facilitate nucleation in the topmost layers of the spin-coated film. Thus, the temperature-assisted approach enables crystallization throughout the whole surface and volume of the mesoporous TiO_2 scaffold and decreases the contribution of voids and SEM-bright, viz. poorly conducting impurities (**Figure 1**a–d). Furthermore, adjusting temperatures used for the hot-casting procedure provides a technically simple means for controlling the impregnation and crystallization of the precursors inside the uneven mesoporous scaffold aiming for the formation of flat and uniform films (Figure S5, Supporting Information). It was additionally noted that the film morphology improves with the amount of copper in Cu_xAgBiI_{4+x}, with the best films obtained at $1.5 \leq x \leq 2.0$, while excessive amounts of Cu ($x > 2.0$) induce undesirable agglomeration of grains (Figure S6, Supporting Information).

Probing the structure of the Cu_xAgBiI_{4+x} films produced by the optimized solution-based hot-casting method with X-ray diffraction revealed that the materials present a composition-dependent combination of two *R*-3*m* space group phases with edge-sharing octahedra[24] (**Figure 2**a). When using a precursor solution with $x = 1$, a rhombohedral $CuAgBiI_5$ with 3D spinel octahedra was a dominant phase. Increasing the Cu:Au ratio beyond 1 resulted in the emergence of the Cu_2AgBiI_6 $CdCl_2$-type layered phase and a progressive decrease in the intensity of the $CuAgBiI_5$ diffraction signals (Figure 2a). It is worth noting that no admixtures of CuI or AgI were detected in all samples examined herein, contrasting the results typically obtained for Ag-rich or Bi-rich silver bismuth iodides.[5a,6a,7] Furthermore,

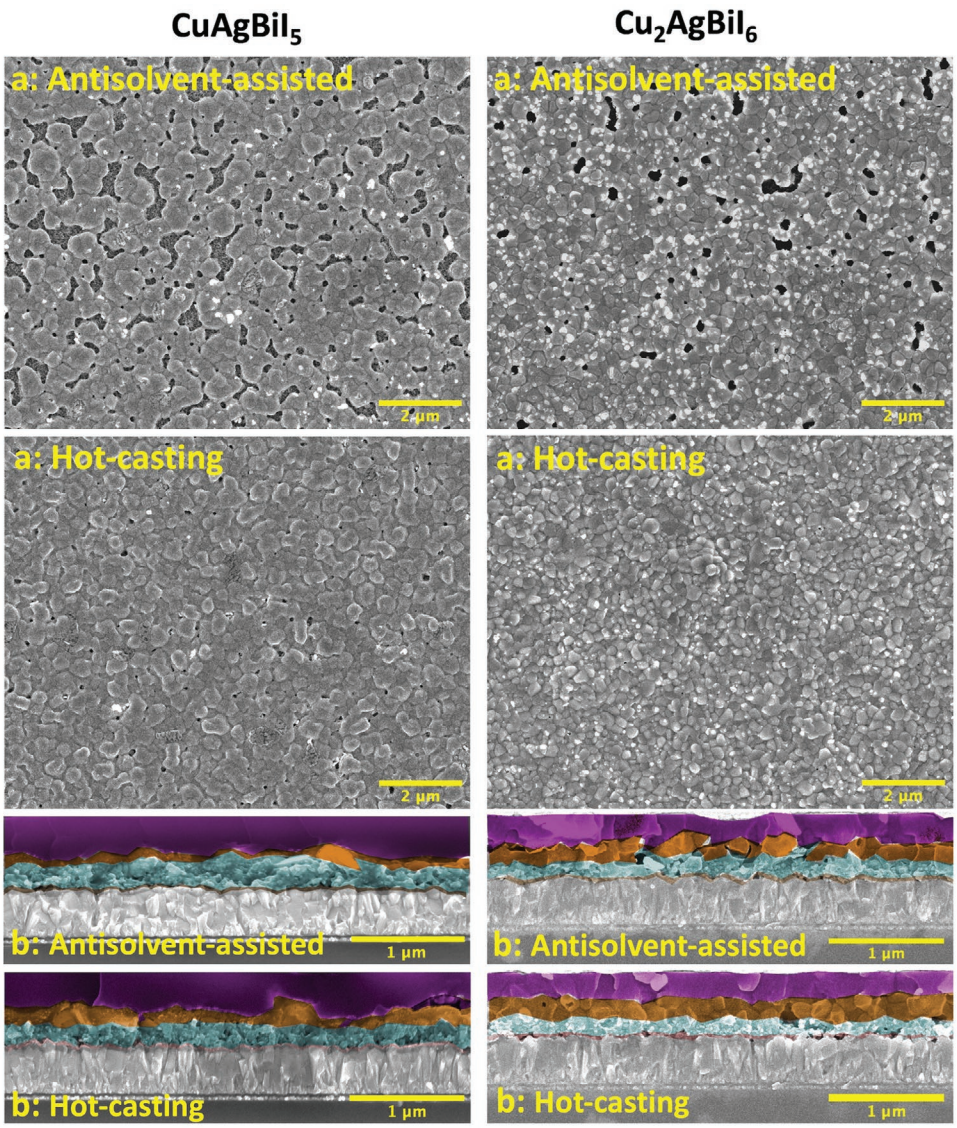

Figure 1. a) Top-view and b) side-view SEM images of the Cu_xAgBiI_{4+x} films with $x = 1$ (left) and 2 (right) deposited via regular antisolvent(chlorobenzene)-assisted spin-coating and hot-casting onto m-TiO_2|c-TiO_2|FTO substrates. Cross-sectional micrographs were recorded for complete devices and were manually colored to highlight the spiro-OMeTAD (purple), Cu_xAgBiI_{4+x} (dark orange), Cu_xAgBiI_{4+x} + m-TiO_2 (teal) and c-TiO_2 (brown) layers on the FTO support.

unlike the case of $AgBiI_4$, which demonstrates cubic (*Fd*3*m*) and $CdCl_2$-type *R*-3*m* space grouped twinned structures, crystal twinning was not observed for the Cu_xAgBiI_{4+x} system herein, which either contained pure ($x = 1$ and $x \geq 2$) or two mixed phases ($1 < x < 2$) (Figure 2a). Relative intensities of XRD peaks for individual phases ($x = 1$ and 2) were different from those reported by Sansom et al.[23] for materials synthesized by high-temperature fusing, reflecting different crystal orientations in thin-film materials, which are often affected by the support.[28] This prevented conventional fitting of the XRD profiles with the tabulated data. It was also noted that the diffractograms for the Cu_xAgBiI_{4+x} films could not be fitted by linear combinations of the data recorded herein for $CuAgBiI_5$ and Cu_2AgBiI_6, which indicates that the structural features of one phase are affected by intermixing with another. Most importantly, the XRD data unambiguously demonstrate a compositionally-controlled transformation from 3D $CuAgBiI_5$ to 2D Cu_2AgBiI_6 (Figure 2b and Figure S8, Supporting Information).

X-ray photoelectron spectroscopic (XPS) analysis confirmed the presence of copper, silver, bismuth, and iodine species on the film surfaces, as well as the change in atomic ratios of the elements corresponding to the transformation from $CuAgBiI_5$ to Cu_2AgBiI_6 (**Figure 3**a–d and Figure S9, Supporting Information). While Ag^+, Cu^+ and I^- were detected as the only states of these elements, which did not change with increasing *x*, the dominating Bi^{3+} signals in the Bi 4f spectra (164.6 and 159.4 eV) were accompanied by low-intensity signals with binding energies close to metallic bismuth (Figure 3c and Figure S10, Supporting Information). The appearance of these "Bi^0" species could be due to a high concentration of interstitial defects, viz. absence of

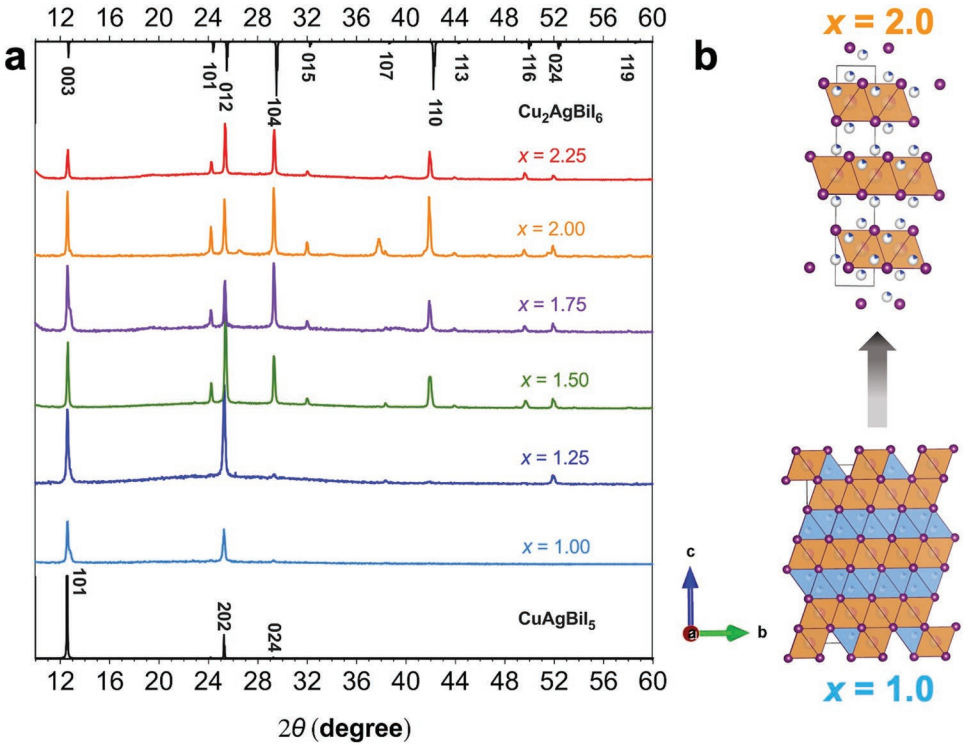

Figure 2. a) XRD patterns of the Cu_xAgBiI_{4+x} films on glass with $x = 1$ (light blue), $x = 1.25$ (blue), $x = 1.5$ (green), $x = 1.75$ (purple), $x = 2$ (orange), and $x = 2.25$ (red); black curves show XRD patterns for $CuAgBiI_5$ (2107463 entry ID) to Cu_2AgBiI_6 (2107468 entry ID) deposited by Sansom et al.[23,24] to the Cambridge database. b) Structures of 3D $CuAgBiI_5$ ($x = 1$) and 2D Cu_2AgBiI_6 ($x = 2$).

some of the Bi—I bonds typically observed in BiI_3.[25] It is also vital that XRD did not provide any evidence for significant crystallographic defects in the materials examined herein, suggesting that the "Bi^0" species might be predominantly surface-confined.

The surface composition of the Cu_xAgBiI_{4+x} materials with $x = 1$ and 2 derived from XPS was in satisfactory agreement with the expected stoichiometry (Figure 3e and Table S1, Supporting Information). It is also noted that essentially the same elemental ratios were measured for the samples deposited by conventional antisolvent-assisted spin-coating with poor morphology (Figure S11, Supporting Information). In addition, bulk metal ratios determined by inductively coupled plasma optical emission spectroscopy (ICP-OES) also conformed to the expected $CuAgBiI_5$ and Cu_2AgBiI_6 compositions (Figure 3e).

Overall, physical characterization demonstrates that the employed hot-casting method enables formation of the Cu_xAgBiI_{4+x} materials with phase composition and dimensionality directly controlled by the amount of Cu introduced. The films produced uniformly cover the titania-based substrate as required for optoelectronic applications.

2.2. Optoelectronic Properties

Effects of the phase composition and dimensionality on the optical properties of Cu_xAgBiI_{4+x} were analyzed and compared to those of the well-explored double perovskite, $Cs_2AgBiBr_6$. The light-harvesting capability was significantly improved for $CuAgBiI_5$ and Cu_2AgBiI_6 with red-shifted and broadened absorption as compared to $Cs_2AgBiBr_6$ (**Figure 4**a and Figure S12, Supporting Information). Analysis of materials obtained by reacting [KI + AgI +BiI_3] and [RbI + AgI + BiI_3] produced optical absorption with several peaks between 500 and 550 nm, probably contributed by the lower-dimensional bismuth perovskites (Figure S12a, Supporting Information), confirming the XRD results on the phase segregation.

Cu_2AgBiI_6 films demonstrated broader absorption than $CuAgBiI_5$ with no well-defined peaks (Figure 4a). The optical absorption covered almost the entire visible spectra with a cut-off around ≈680 and 700 nm for $CuAgBiI_5$ and Cu_2AgBiI_6, respectively. Slightly broader absorption was reported for $CuAgBiI_5$ by Sansom et al. for the materials obtained by high-temperature synthesis.[24] Herein, improved absorption is demonstrated by 3D $CdCl_2$-type $CuAgBiI_5$ at shorter wavelengths (<480 nm) alongside a small unknown peak at ≈420 nm (Figure 4a and Figure S12b, Supporting Information). It is additionally noted that absorption coefficients measured herein are slightly higher than those reported before,[24] which can be attributed to improvements in the film compactness and slightly lower direct bandgap values.

Examination of the optical absorption edges in the $(\alpha h\nu)^n$–$h\nu$ Tauc coordinates revealed that Cu_xAgBiI_{4+x} are direct bandgap photoactive semiconductors with E_g of 1.94 ± 0.05 eV for $CuAgBiI_5$ and 1.89 ± 0.05 eV for Cu_2AgBiI_6 (Figure 4a). Photoelectron spectroscopy in the air (PESA) studies also produced slightly different valence band edge (E_{VB}) values of –5.16 ± 0.05 eV for $x = 1$ and –5.25 ± 0.05 eV at $x = 2$ (Figure 4b and Figure S13, Supporting Information). These

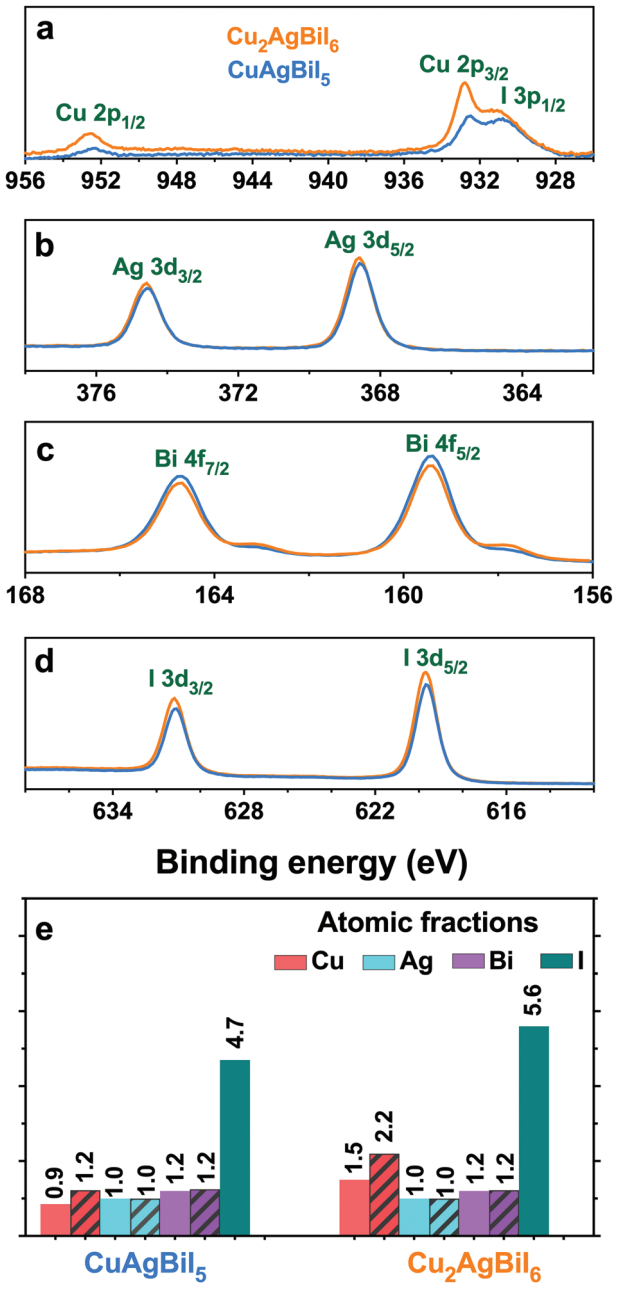

Figure 3. High resolution a) Cu 2p + I 3p, b) Ag 3d, c) Bi 4f, and d) I 3d spectra of Cu_xAgBiI_{4+x} with $x = 1$ (light blue) and 2 (orange), and e) corresponding atomic fractions derived from XPS (solid) and ICP-OES analysis (hashed).

results indicate that the effects of the lower-dimensional A-site cations on band edges and electronic structure are not strong, in contrast to the Bi and I valence states.[4c] Sansom et al. also observed similarly small differences in E_g and E_{VB} between $CuAgBiI_5$ and Cu_2AgBiI_6. However, the band level values were different from those obtained herein, probably due to the use of distinct measurement methods and synthesis conditions.[24] When comparing the results obtained for the Cu_xAgBiI_{4+x} system to the optoelectronic structure of $Cs_2AgBiBr_6$ (E_g = 2.37 eV, E_{VB} = −5.56 eV) and the density of states reported for Cu_xAgBiI_{4+x} materials,[24] one can conclude that the A-site cationic (Cs^+ to Cu^+) and X-site anionic (Br^- to I^-) modification collectively induce several important changes, viz. transition from indirect to direct band semiconductor with considerably improved light absorption and upshifted valence band.

The valence band edges were slightly-off for $CuAgBiI_5$ (−5.16 eV) and closely aligned for Cu_2AgBiI_6 (−5.25 eV) against the highest occupied molecular orbital (HOMO) of the conventional hole transport material spiro-OMeTAD (−5.20 eV).[29] This can be resolved by employing other hole transport materials and modifying the band level of spiro-OMeTAD by deeper doping with spiro-OMeTAD$(TFSI)_2$ (Figure 4b and Figure S13, Supporting Information). Calculated conduction band edges (E_{CB}) were −3.22 and −3.35 eV for $CuAgBiI_5$ and Cu_2AgBiI_6, respectively, leaving a significant gap from the conduction band edge of the conventional TiO_2 electron transport material (−4.20 eV),[29] signifying possible trap-state recombination during the charge transfer.

Like many bismuth-based lead-free perovskite-inspired materials, Cu_xAgBiI_{4+x} demonstrates weak photoluminescence (PL), which was very similar for $x = 1$, 1.5, and 2 (Figure 4c and Figure S14a, Supporting Information). The PL signal decay was found to decay mono-exponentially with a carrier lifetime of 1.3 ± 0.1 µs, which was essentially unaffected by x (Figure 4d and Figure S14b, Supporting Information). In contrast, PL decay transients for $Cs_2AgBiBr_6$ are best fitted by a biexponential dependence with a prominent short-lifetime (<10 ns) component (Figure 4d and Figure S14, Supporting Information). No significant differences in the PL properties of $CuAgBiI_5$ and Cu_2AgBiI_6 were found even at a higher fluence (Figure S15, Supporting Information). These results indicate that the PL properties of the Cu_xAgBiI_{4+x} films are effectively independent of phase dimensionality.

Interestingly, using the hot-casting method, the PL spectra of $CuAgBiI_5$ and Cu_2AgBiI_6 films deposited on glass substrates show excellent stability for 22 h under ambient laboratory conditions (Figure S16, Supporting Information), contrasting previous reports of a blue shift and intensification of the PL spectra upon exposure to air.[24] It should be noted that all PL data reported in the present work were measured in air, while Sansom et al.[24] conducted their $t = 0$ measurements in vacuum. No significant change in the PL of Cu_xAgBiI_{4+x} materials over 22 hours of air exposure (Figure S16, Supporting Information) indicates that passivation of the trap-states that suppress non-radiative recombination does not occur under these conditions. This can be either attributed to the effects of the employed processing procedure and/or rapid air-passivation of the materials upon initial exposure to air prior to the PL measurements.

Electron-beam-induced current (EBIC) measurements were undertaken to investigate the carrier diffusion lengths for the Cu_xAgBiI_{4+x} materials (Figure 4e–g). In these experiments, numerous electron–hole pairs are generated in semiconductors by a highly energetic electron beam (electron-voltaic effect rather than photovoltaic), which are later extracted and collected at the electrodes by applying an internal electric field. Thus, imaging of the localized charge carrier generations reveals important electrical features such as the minority carrier diffusion under applied voltage, p–n junction formation within devices, and recombination centers if the crystal grain boundaries are

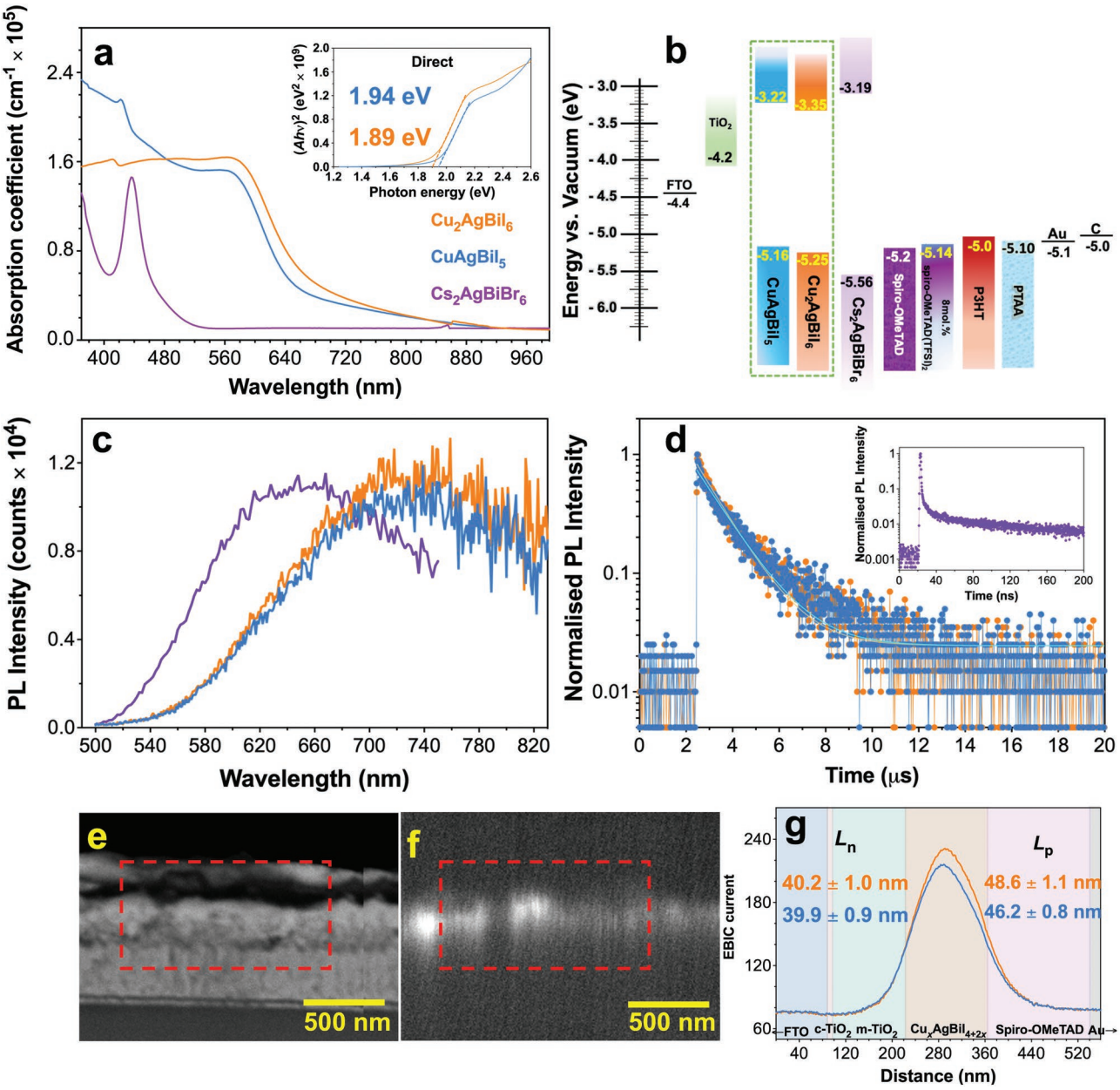

Figure 4. Optoelectronic properties of Cu_xAgBiI_{4+x} with $x = 1$ (light blue) and 2 (orange) (data for $Cs_2AgBiBr_6$ are provided in purple for comparison): a) UV–vis spectra and Tauc plots (inset) (on $mTiO_2|cTiO_2|FTO$); b) valence band edge values (E_{VB}) derived from photoelectron spectra (PESA) (glass-coated samples) along with calculated conduction band edge data compared to energy levels of TiO_2 and HTMs; c) photoluminescence spectra, and d) photoluminescence decay measurements (λ_{ex} = 465.8 nm; glass-coated samples) (inset shows TRPL profile for $Cs_2AgBiBr_6$); cross-sectional e) secondary electron image and f) EBIC image under internal electric field for complete $Au|spiro\text{-}OMeTAD|Cu_2AgBiI_6|m\text{-}TiO_2|c\text{-}TiO_2|FTO$ devices, and g) EBIC profiles for Cu_xAgBiI_{4+x} with $x = 1$ (light blue) and 2 (orange) integrated over relevant areas in the images (exemplified for Cu_2AgBiI_6 with dashed lines in panels e,f); background shading shows layers within the devices.

visible. It can be considered that electrons and holes are generated as free charge carriers considering that the applied energy (>0.05 eV) significantly exceeds the exciton binding energy. Within complete solar cell devices, internal electric fields and the field created by the external bias would contribute to the carrier generation minimizing the photoinduced exciton generation.

Cross-sectional images and corresponding EBIC profiles of the devices reveal localized charge carrier generation within the active material (Figure 4e,f and Figure S17, Supporting Information). The integrated profiles extracted from the EBIC images demonstrated the current probe peaking at the center of the Cu_xAgBiI_{4+x} layer, indicating the formation of a p–i–n structure (Figure 4g). The difference in the EBIC current intensity provides a measure of the carrier dynamics. Specifically, we observe a gradual improvement in the EBIC values from the $HTM|Cu_xAgBiI_{4+x}$ and $ETM|Cu_xAgBiI_{4+x}$ interfaces toward the active layer (Figure 4g) and increased intensity around larger compared to the less connected smaller grains (Figure 4e,f).

The latter observation indicates that the grain boundaries and interfaces rather than the layer surface are active channels for the carrier extraction and collection. The electron diffusion lengths (L_n) derived from the EBIC data for $CuAgBiI_5$ and Cu_2AgBiI_6 were 40 ± 1 and 46 ± 1 nm, while the hole carrier diffusion lengths (L_p) were around 40 ± 1 nm and 49 ± 1 nm, respectively (Figure 4e–g and Figure S18a–c, Supporting Information). Considering the amount of drift in EBIC current while imaging, these values could be slightly underestimated. However, comparing these values to the active layer thickness of 120–150 nm above the *m*-TiO_2 network implies that a thinner and compact active layer could avoid potential recombination in the devices and thereby enhance the efficient extraction of charges. However, attempts to develop thinner layers resulted in non-uniform coverage of the films at this stage (Figure S19, Supporting Information).

2.3. Photovoltaic Performance

Solar cells based on the hot-casted Cu_xAgBiI_{4+x} films had a n–i–p architecture C|HTM|Cu_xAgBiI_{4+x}|m-TiO_2|c-TiO_2|FTO (Figure 1b). The use of c-TiO_2|FTO without a mesoporous titania layer did not produce high-quality films regardless of the deposition conditions used (exemplified in Figure S19, Supporting Information). Corresponding devices expectedly produced much worse photovoltaic performance than the m-TiO_2|c-TiO_2|FTO-based ones (Figure S20 and Table S2, Supporting Information). It was also found that conventional LiTFSI, *t*BP, and FK209 cobalt(III) complex additives to spiro-OMeTAD have a strongly adverse effect on the active layers (Figure S21, Supporting Information), which motivated us to use [spiro-OMeTAD^{2+}][TFSI]$_2$ as a chemically cleaner dopant, following procedures established in our laboratories.[30] The best performance was achieved by adding 8 mol% of spiro-OMeTAD^{2+} with respect to spiro-OMeTAD^0, resulting in a HOMO level of –5.14 eV. Other HTMs such as PTB7 (HOMO = –5.2 eV),[29] PTAA (HOMO = –5.1 eV),[6a] P3HT (HOMO = –4.8 eV),[31] and Fe(bpyPY4)](OTf)$_{2+x}$ (HOMO = –5.4 eV)[32] were also examined, but all provided inferior results to those obtained with 8 mol.% spiro-OMeTAD^{2+} doped spiro-OMeTAD (Figure S22 and Table S3, Supporting Information). The latter HTM was used for all major experiments discussed below.

A recently developed cheap adhesive carbon counter electrode[33] was used herein and provided significantly better performance than conventional evaporated gold (Figure S23 and Table S4, Supporting Information). This might be possibly attributed to the penetration of evaporated gold through the nanoscale pin-holes within a HTM layer and further through the active layer stimulating the Ag^+ or Cu^+ ion migration.

Photocurrent–voltage (*J–V*) curves recorded from open-circuit to short-circuit (forward bias) and short-circuit to open-circuit (reverse bias) at a scan rate of 0.200 V s^{-1} showed negligible hysteresis (**Figure 5**a). A substantial improvement in the open-circuit voltage (V_{oc}) and short-circuit photocurrent density (J_{sc}) was observed for Cu_xAgBiI_{4+x}-based solar cells with the increase in *x*, peaking the performance at $x = 2$, corresponding to the pure 2D Cu_2AgBiI_6 phase (Figure 5a and Table S5, Supporting Information). The quasi-steady-state photocurrent density tracking at a constant potential corresponding to the maximal power output in the *J–V* curves over 300 s for Cu_2AgBiI_6, which provides a reliable measure of the initial performance of the devices, produced PCE values (2.39 ± 0.05%) similar to those derived from transient *J–V* measurements (2.35 ± 0.04%).

The better performance of 2D Cu_2AgBiI_6 as compared to 3D $CuAgBiI_5$ is consistent with the slightly better film quality (Figure 1) on the m-TiO_2|c-TiO_2|FTO support, broadened optical absorption (Figure 4a), better-aligned energy levels (Figure 4b), and slightly improved carrier lifetime (Figure 4d). The PCE and J_{sc} achieved herein for Cu_2AgBiI_6 compare well to those reported for $Cs_2AgBiBr_6$ combined with similar ETM and HTM and are better than those provided by a range of other lead-free perovskite-inspired materials (Table S6, Supporting Information).[6a,13a,27,34] Furthermore, the photovoltaic metrics presented in this work are the best reported to date for the Cu_xAgBiI_{4+x} class of materials. As anticipated, the films produced with the solution and substrate temperatures of 100 °C produced the best results among the devices based on the Cu_xAgBiI_{4+x} films prepared using hot-casting and were also better than those achieved when using antisolvent-assisted spin-coating (Figure S24, Supporting Information). These results emphasize the importance of film quality for photovoltaic performance.

Profiles of the incident photon to current conversion efficiency (IPCE) spectra (Figure 5b) were qualitatively consistent with the optical absorption data (Figure 4a and Figure S25, Supporting Information) but quantitatively different, showing significantly higher IPCE for Cu_2AgBiI_6 within the whole wavelength range examined. The IPCE recorded for the Cu-rich material was lower than those reported for the $Ag_aBi_bI_{a+3b}$-PTAA-based solar cells,[6–8] but comparable to other bismuth-based perovskite-inspired materials.[4c,16a,35]

Dependencies of the short-circuit current and open-circuit voltage on the light intensity were linear in the semi and bilogarithmic coordinates, respectively, confirming the charge extraction capability at varying illumination (Figure 5c). The J_{sc} plots displayed the same slope of ≈1.0 for $CuAgBiI_5$ and Cu_2AgBiI_6. On the other hand, the ideality factors derived from the V_{oc} versus light intensity data were distinctly different, viz. 1.3 and 2.7 for $CuAgBiI_5$ and Cu_2AgBiI_6, respectively. These values suggest multiple trapping in band edge states or tail states, thereby mediating trap-assisted (SRH) recombination.[36]

To further understand the performance-limiting parameters, impedance spectroscopy was applied to investigate the charge transfer within the devices as a function of the dimensionality and phase composition defined by the change in the copper(I) concentration. Experimental data for the devices based on both $CuAgBiI_5$ and Cu_2AgBiI_6 were found to be well described by a simple $R_s[R_{rec}\|CPE]$ equivalent circuit, where R_s is series resistance, CPE is a constant phase element used to model the capacitive behavior of the device, and R_{rec} is recombination resistance (Figure S26, Supporting Information). Hence the charge transfer within the Cu_xAgBiI_{4+x}-based devices is governed by recombination at one of the critical interfaces, described by the parallel capacitor and resistor elements. It is worth noting that from Nyquist plots (Figure S26a, Supporting Information), we have found a small inductive loop at low frequencies below 10 Hz, which suggests that ion migration might

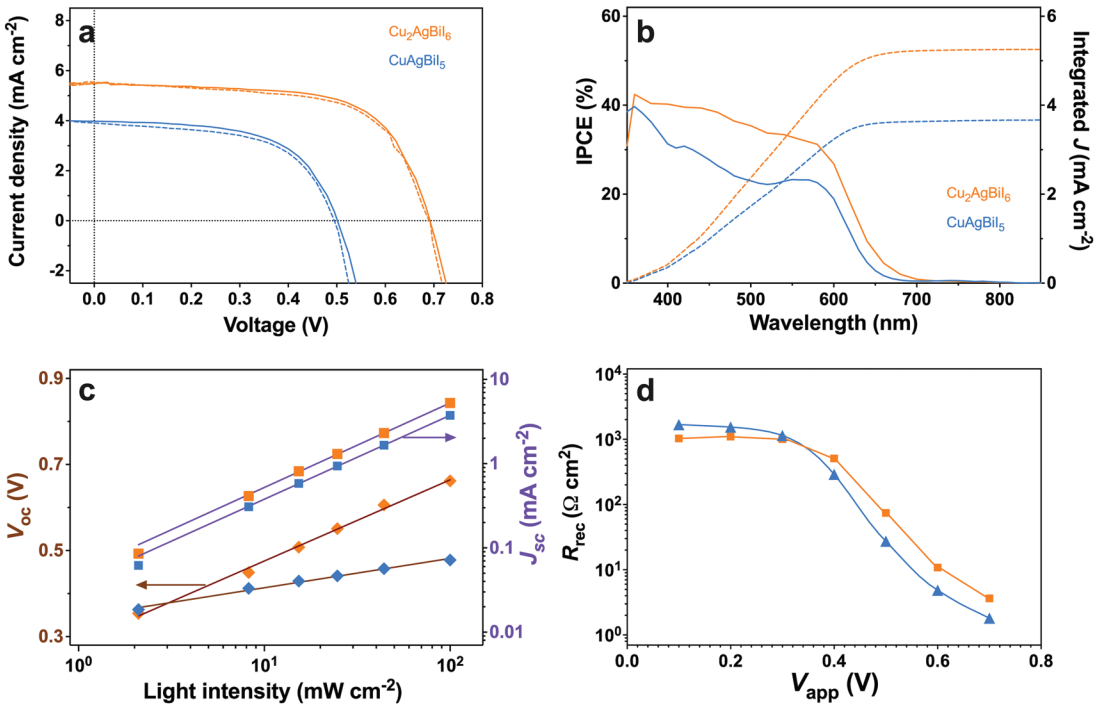

Figure 5. Photovoltaic performance of the C|spiro-OMeTAD|Cu_xAgBiI_{4+x}|m-TiO_2|c-TiO_2|FTO solar cells (aperture 0.16 cm^2) with $x = 1$ (light blue) and 2 (orange): a) photocurrent density versus voltage curves (sweep rate 0.200 V s^{-1}; 1 sun AM 1.5G irradiation) recorded in the open-circuit to short-circuit (solid) and short-circuit to open-circuit (dashed) (dotted lines are guides to the eye showing zero J and V); b) IPCE spectra (solid) and corresponding integrated photocurrent (dashed); c) dependence of the open-circuit voltage (V_{oc}) and short-circuit photocurrent (J_{sc}) on the illumination light intensity (note semi-log coordinates for V_{oc} and bilogarithmic coordinates for J_{sc}), and d) recombination resistance, R_{rec} extracted from the impedance spectroscopic analysis (lines are guides to the eye); Nyquist plot with the equivalent circuit used for the fitting and other parameters obtained are shown in Figure S25 and Table S6 in the Supporting Information.

still exist in the Cu_xAgBiI_{4+x} materials, but much slower than in the lead-halide perovskites.

As expected, the R_{rec} values were found to decrease with increasing the applied voltage (Figure 5d, Table S7 and Figure S26b, Supporting Information).[37] R_{rec} is smaller for the devices based on $CuAgBiI_5$ as compared to the Cu_2AgBiI_6-based ones within the voltage range of 0.4–0.7 V, consistent with the lower V_{oc} for the 3D material (Figure 5a). This result was corroborated by the J–V data obtained from the impedance fitting (Figure S27, Supporting Information). The geometric capacitance was very similar for all devices examined (Figure S26d, Supporting Information), indicating similar dielectric constants of the active layers with different phase compositions.

The effect of x on the photovoltaic performance of the Cu_xAgBiI_{4+x} materials was analyzed for 24 devices of each type to ensure consistency of the established trends (**Figure 6** and Table S5, Supporting Information). As x increased from 1 to 1.75, open-circuit voltage improved steadily though to a small extent from 0.46 ± 0.03 to 0.53 ± 0.06 V, but abruptly changed to a significantly higher value of V_{oc} = 0.70 ± 0.03 V at $x = 2$, i.e., when a pure Cu_2AgBiI_6 phase was formed (Figure 6a). In contrast, the short-circuit current density followed a close to linear dependence on x within the 1–2 range changing from 3.5 ± 0.3 to 5.2 ± 0.2 mA cm^{-2} (Figure 6b). The fill factor also improved from 0.59 ± 0.05 at $x = 1$ to 0.67 ± 0.04 at $x = 2$ (Figure 6c) and did not demonstrate any abrupt changes upon the formation of a pure 2D structure. These trends were corroborated by the PCE values derived from the steady-state power output measurements (Figure 6e). The increase in V_{oc} with x can be attributed to the improved film coverage that reduces surface defects and band alignment with the interfacial layers and avoids trap-assisted recombination while broadening the light absorption. Higher IPCE of Cu_2AgBiI_6 promotes improvements in J_{sc} with x. An increase in x beyond 2 induces a slight drop in the photovoltaic performance, which might be due to uneven crystal growth, deterioration of the film morphology, and the presence of impurities on the surface (Figure S6, Supporting Information). However, a higher fill factor was obtained for the films with x = 2.25 (Figure 6c), probably due to improved interfacial contact.

The best-performing devices based on $CuAgBiI_5$ exhibited a V_{oc} = 0.49 V, J_{sc} = 3.93 mA cm^{-2}, FF = 0.63, and a corresponding PCE of 1.21%, and Cu_2AgBiI_6 exhibited a V_{oc} = 0.71 V, J_{sc} = 5.3 mA cm^{-2}, FF = 0.65, and a corresponding PCE of 2.45%. Considering the S–Q limit, $CuAgBiI_5$ and Cu_2AgBiI_6 have the potential to provide up to ≈24% and ≈25% PCE at the radiative limit, with a V_{oc} of 1.64 and 1.59 V, J_{sc} of 16.0 and 17.2 mA cm^{-2}, and a FF of 0.92. While the FF obtained for the devices is reasonably good with a <25% loss, there is a significant loss in V_{oc} and J_{sc}.[38] This could be due to a range of factors, including low diffusion length even while having a longer carrier lifetime, implying possibly low intrinsic carrier mobilities, flat bands with not favorable electronic structure, and higher built-in potential due to improper band alignment with the charge-transport layers. Most of these constraints can

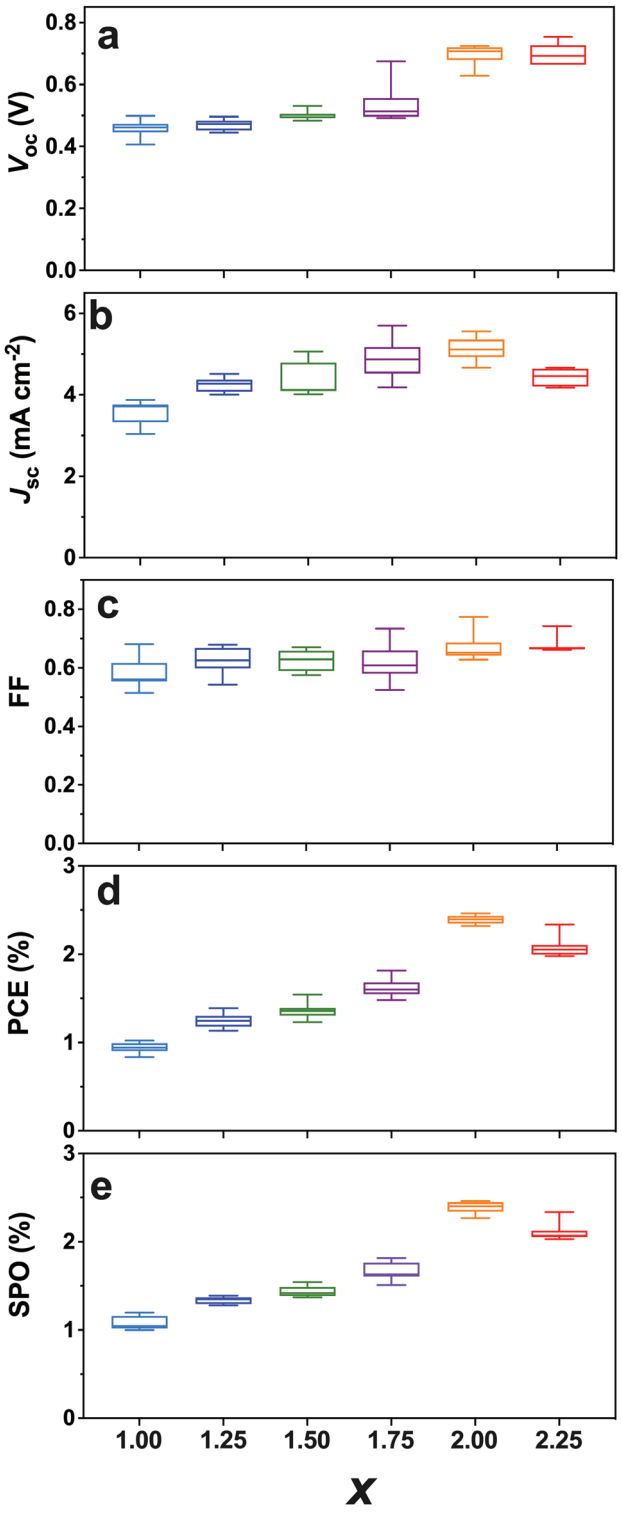

Figure 6. Influence of the composition of Cu_xAgBiI_{4+x} on the major photovoltaic parameters of the C|spiro-OMeTAD|Cu_xAgBiI_{4+x}|m-TiO_2|c-TiO_2|FTO solar cells (aperture 0.16 cm^2): a) open-circuit voltage, b) short-circuit current density, c) fill factor, d) power conversion efficiency, and e) the steady-state power output. Data were derived from a–d) *J–V* curves and e) quasi-steady-state measurements recorded under 1 sun AM1.5G irradiation (as demonstrated in Figure 5) for 24 independent solar cells of each type.

be resolved by employing thinner compact layers and utilizing better-aligned charge transport layers, e.g., an ETM with a more positive conduction band.

2.4. Environmental Stability

When stored in air under ambient conditions (24 ± 2 °C, relative humidity 10–20%) and diffuse light, the Cu_xAgBiI_{4+x} films with $x \leq 1.5$ (supported on m-TiO_2|c-TiO_2|FTO) suffer visually detectable degradation, viz. change in color from dark purple to dark red and then to yellow on a timescale of days (**Figure 7**a). While the XRD patterns of the aged material still exhibited the peaks associated with the copper-silver-bismuth iodide phase(s), an unknown peak at 10.7° emerged, and the intensity of the (101) peak reduced slightly during storage in air (Figure 7a). Contrasting this behavior, no visible changes were observed for the films with $x > 1.5$ and containing a higher amount of 2D Cu_2AgBiI_6 (Figure 7b). The significantly higher stability of the 2D structure as compared to the 3D one is consistent with the observations reported by Sansom et al.[24]

Interestingly, these differences in the stability of materials were not translated to the long-term storage stability of the non-encapsulated devices under ambient conditions and diffuse light, which did not lose significant performance over 240 days (Figure 7c). During the initial 100 days, both the $CuAgBiI_5$ and Cu_2AgBiI_6 devices retained over 90% of the efficiency; however, over the next 140 days, the $CuAgBiI_5$ devices lost almost 15% of their initial efficiency. The Cu_2AgBiI_6 devices retained over 80 % of the initial efficiency after these 8 months. The improvement in the performance during the initial 7 days of storage might be associated with the beneficial surface passivation that suppresses the ion-migration-induced defects, although there might be other factors contributing.[39] It was also found that devices with $CuAgBiI_5$ as an active layer demonstrated loss in the performance under continuous irradiation, which was not the case for the Cu_2AgBiI_6-based solar cells, which were perfectly stable in operation (Figure 7d).

The impressive environmental stability of the devices indicates that other cell components provide sufficiently adequate protection of the active layer from the degradation-inducing reactions with the ambient atmosphere. At the same time, the Cu_2AgBiI_6-based devices with P3HT as a hole-transporting material suffered degradation at the gold-HTM interface, probably due to the Ag^+ and Bi^+ ion migration (Figure S28, Supporting Information).[40] Importantly, this unfavorable phenomenon was not observed with the carbon electrode-based devices and solar cells with a Au electrode and other HTMs.

3. Conclusions

The present work presents a comprehensive study on the compositional control of the phase, dimensionality, and optoelectronic properties of the solution-processed Cu_xAgBiI_{4+x} thin films. We demonstrate a correlation between x and the ratio of the two major phases—3D $CuAgBiI_5$ and 2D Cu_2AgBiI_6, and corresponding changes in the light absorption. The latter is significantly better for Cu_xAgBiI_{4+x} as compared to the archetypal

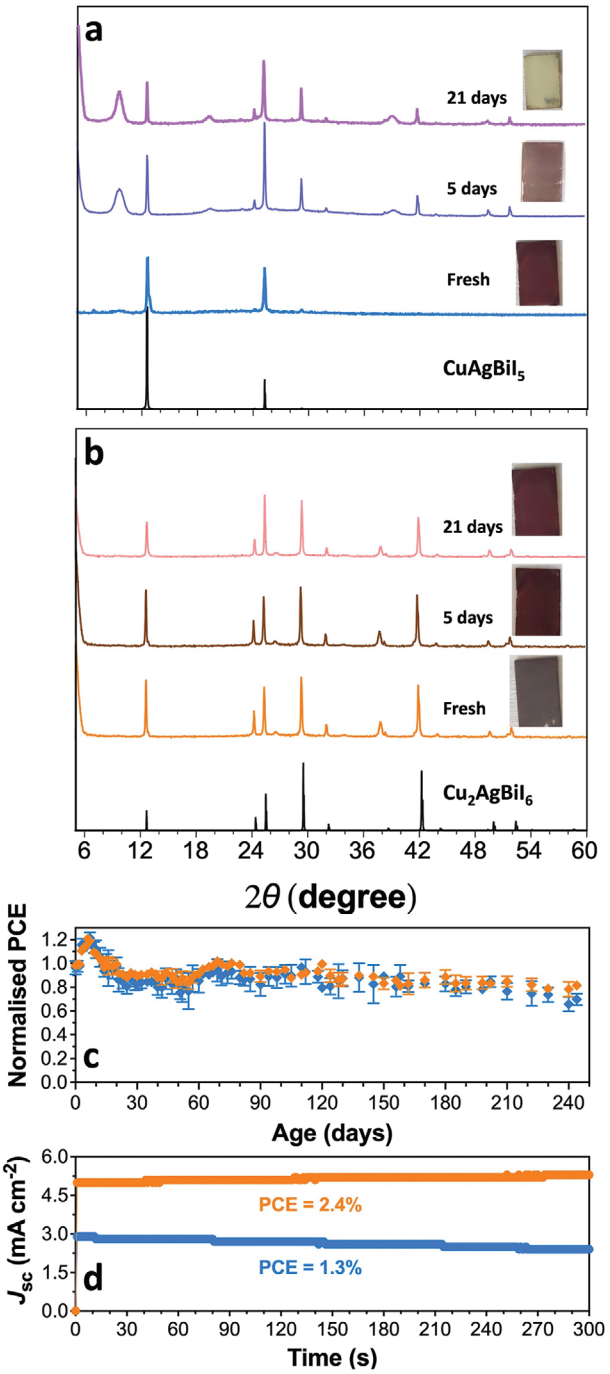

Figure 7. XRD patterns and photographs of aged a) $CuAgBiI_5$ and b) Cu_2AgBiI_6 thin films deposited on glass. c) Evolution of normalized PCE of the C|spiro-OMeTAD|Cu_xAgBiI_{4+x}|m-TiO_2|c-TiO_2|FTO solar cells (aperture 0.16 cm^2) with $x = 1$ (light blue) and 2 (orange) stored in air under diffuse light. d) Photocurrent transients recorded at potentials of maximal power derived from *J–V* data for the devices tested with an aperture of 0.16 cm^2.

$Cs_2AgBiBr_6$ double-perovskite, demonstrating how the simultaneous A-site cationic and anionic substitution can deliver a new photovoltaic material with improved optoelectronic characteristics while maintaining the high robustness of the parent compound. This partially addresses the impossibility of the highly desired but unachievable direct Br^--to-I^- anionic modification in $Cs_2AgBiBr_6$. Our results also demonstrate that the change in the dimensionality in the Cu_xAgBiI_{4+x} system from 3D to 2D decreases the bandgap to expand the light absorption by the material to almost the whole visible spectrum and downshifts the valence band level.

Another feature of the present work is the first demonstration of a solution-based method for synthesizing thin films of Cu_xAgBiI_{4+x} with controlled composition by the hot-casting approach. Hot-casting-assisted spin-coating improves crystallization control and produces uniformly covered and well-connected Cu_xAgBiI_{4+x} films with suppressed surface defects. Solar cells produced using this method demonstrated high storage stability and delivered power conversion efficiencies of up to 1.3% and 2.4% for $CuAgBiI_5$ and Cu_2AgBiI_6-based devices, respectively. These are the best performances of these materials reported to date. Nevertheless, the advantages of Cu_2AgBiI_6 compared to $Cs_2AgBiBr_6$ demonstrated herein are not as significant as the differences in the optoelectronic properties of the two materials. One aspect that might be optimized in the future is the thickness of the active Cu_2AgBiI_6 layer to better match the minority carrier diffusion lengths in the range of 40–50 nm measured herein. The use of dopants to improve the carrier mobility and appropriate charge transport layers that could match the positive conduction band of Cu_xAgBiI_{4+x} is expected to address the voltage and current loss issues. Finally, computational and experimental exploration of related A_xBMX_{4+x} compositions might unveil new promising materials, of which compounds with a wider direct bandgap might be used as components of the tandem solar cells.

4. Experimental Section

Materials: Copper(I) iodide (≥99.5%), silver(I) iodide (99%), bismuth(III) iodide (99%), anhydrous dimethylsulfoxide (DMSO; 99.9%), anhydrous *N,N*-dimethylformamide (DMF; 99.8%), anhydrous chlorobenzene (CBz; 99.9%) anhydrous toluene (99.8%), titanium diisopropoxide bis(acetylacetonate) solution (TAA) (75 wt% in isopropanol), lithium bis(trifluoromethane)sulfonimide (LiTFSI; >99%), 4-*tert*-butylpyridine (t-BP; 98%), tris-2-(1H-pyrazol-1-yl)-4-tert-butylpyridine)cobalt(III) tri[bis(trifluoromethane)sulfonimide] (FK209; 98%), and poly[bis(4-phenyl)(2,4,6-trimethylphenyl)amine] (PTAA; M_n = 7000–10 000) were purchased from Sigma-Aldrich. 2,2′,7,7′-Tetrakis(N,N-di-p-methoxy phenylamino)-9,9 spirobifluorene (spiro-OMeTAD) was purchased from Luminescence Technology Corp. 2,2′,7,7′-Tetrakis(N,N-di-p-methoxy phenylamino)-9,9 spirobifluorene bis(trifluoromethane) sulfonimide (spiro-OMeTAD$(TFSI)_2$) and (6,6′-bis(1,1-di(pyridin-2-yl)ethyl)-2,2′-bipyridine)-iron(II/III) trifluoromethanesulfonate ([Fe(bpyPY4)]$(OTf)_{2+x}$) were synthesized following the reported procedures.[32] Titania particle paste (average size 30 nm; 30 NRD) was purchased from GreatCell Solar Materials Ltd. Absolute ethanol was purchased from UNIVAR solutions. Poly(3-hexylthiophene-2,5-diyl (P3HT) was purchased from Rieke Metals. Water purified by reverse osmosis (quoted resistivity 1 MΩ cm) was used in all experimental procedures whenever water is mentioned. High purity N_2 (≤ 2 ppm O_2, ≤ 0.1 ppm H_2O) and Ar (< 3 ppm O_2, < 0.2 ppm H_2O) were used.

Fluorine-doped tin (IV) oxide (FTO) coated glass substrates with the size of 2.5 cm × 2.5 cm having a sheet resistance of 15 Ω sq^{-1} were purchased from Yingkou Shangneng Photoelectric material Co., Ltd. Microscope-glass substrates of 1–1.2 mm thickness used for the physical

characterization were purchased from Livingstone International Pty. Ltd. 2 vol% Hellmanex III detergent solution was purchased from Helma analytics. Jelcon CH-8 carbon paste was purchased from JuJo Chemicals Co. Ltd. for the carbon electrode preparation. Silver paste (CP1 30J) from ChipQuick and a 12 µm thick domestic grade all-purpose aluminum foil from Castaway Caterers Foil Australia were used as purchased to improve the contact of carbon electrodes.[33]

Photovoltaic Device Fabrication: Cleaning of the pre-patterned FTO-coated glass substrates included sequential ultrasonication (Elmasonic S 300H bath at an operating power of 1500 W) in a 2 wt% Helmanex surfactant solution, water, and ethanol (15 min in each medium), drying under N_2 flow, and plasma treatment at 1000 mTorr for 10 min (Harrick Plasma cleaner PDC-002 at maximum power). A 15 nm thick compact titania blocking layer (c-TiO_2) was formed on a cleaned FTO substrate surface using a custom-made automatic spray pyrolysis system by depositing a 5 vol% TAA precursor in anhydrous isopropanol at 500 °C (heated by high-precision hot-plate Harry Gestigkeit GmbH PZ28-3TD) for 30 min. Upon cooling to ambient temperature, cTiO_2|FTO substrates were covered with a mesoporous titania layer (m-TiO_2; thickness ≈ 150 nm) by spin-coating (4000 rpm for 20 s with a Laurell-150 mm spin-coater) 75 µL of a 30 nm TiO_2 particle paste dispersed in ethanol, followed by drying at 100 °C and sintering at 500 °C in air on a high precision hot-plate (Harry Gestigkeit GmbH PZ28-3TD).

The Cu_xAgBiI_{4+x} precursor solutions were prepared by dissolving copper(I), silver(I), and bismuth(III) iodides to achieve the target [Cu_xAgBiI_{4+x}] concentration of 0.45 M in a DMSO:DMF solvent mixture (optimized ratio 3:1 vol) for 1 h under vigorous stirring at 100 °C. The obtained solutions were filtered once cooled down and were spin-coated onto 2.5 cm × 2.5 cm FTO-substrates by a two-step programmed spin-coating, where initially the solution was spread by spinning at 1000 rpm for 10 s, followed by 6000 rpm for 20 s. For the gas-assisted deposition, Ar gas was flown at 20 mL min^{-1} in the center of the spun sample after 2 s in the second cycle for 15 s. For the antisolvent-assisted deposition, 100 µL of isopropanol, chlorobenzene, diethyl ether, or toluene were decanted into the center of the substrate 5 s before the end of the spinning. For the dynamic hot-casting, the films and substrates were preheated at varying temperatures (60 °C ≤ T ≤ 120 °C) before spin-coating and the solution was deposited at 2 s of the initial spinning cycle.

The resultant films were annealed in an N_2-filled glove box at 80 °C for 2 min, followed by additional heating at 150 °C for 5 min with an IKA RCT basic titanium hot-plate, and then cooled to ambient temperature (24 ± 2 °C) naturally. The 2.5 cm × 2.5 cm Cu_xAgBiI_{4+x} + mTiO_2|c-TiO_2|FTO films were then modified with a hole-transporting material (HTM) layer. Examined HTMs included PTAA, P3HT, spiro-OMeTAD doped with FK209 cobalt complex in the presence of $LiNTf_2$ and *t*BP, spiro-OMeTAD doped with spiro-OMeTAD$(TFSI)_2$, and [Fe(bpyPY4)]$(OTf)_{2+x}$. PTAA was deposited by spin-coating 25 µL of a 10 mg mL^{-1} toluene solution at 1800 rpm for 30 s, then annealing at 60 °C. P3HT was deposited by spin-coating 20 µL of a 15 mg mL^{-1} dichlorobenzene solution at 2000 rpm for 30 s and subsequently annealing at 135 °C. Spiro-OMeTAD was deposited by spin-coating 30 µL of a solution containing 67.2×10^{-3} M spiro-OMeTAD dissolved in chlorobenzene with 20 mmol *t*BP (28.8 µL), 20 mmol $LiNTf_2$ (17 µL of 520 mg mL^{-1} solution in acetonitrile), and 160 mmol FK209 (8 µL of 300 mg mL^{-1} solution in acetonitrile) at 3000 rpm for 30 s. For the spiro-OMeTAD^{2+}-doped solution, spiro-OMeTAD and spiro-OMeTAD$(TFSI)_2$ with different mole fractions were mixed in chlorobenzene while the total concentration remained at 67.2×10^{-3} M. This solution was vigorously stirred while heating at 70 °C for 30 min to fully dissolve the chemicals and cooled to room temperature before spin coating. [Fe(bpyPY4)]$(OTf)_2$ (21.9 mg) and [Fe(bpyPY4)](OTf)2.9 (25.6) were dissolved in dichlorobenzene (1 mL), and 25 µL of this solution were spin-coated at 2000 rpm for 30 s.

The devices were completed by depositing a counter-electrode, either carbon-based or Au. Adhesive carbon electrodes with a thickness of ≈25 µm were prepared following the reported procedure.[33] Briefly, the electrode was deposited onto a copper-coated aluminum substrate by automated doctor blading (MTVmesstechnik CX202) of ≈ 5 mg cm^{-2} of the Jelcon CH-8 paste at a rate of 9 mm s^{-1} and height adjusted to 80 µm. The resulting electrodes were immersed in stirred ethanol for 30 min to remove additives in the commercial carbon paste and dried in the ambient environment for 2 h at 65 °C. After cooling, the electrodes were cut to a size of 0.5 cm × 0.5 cm and applied to four devices simultaneously using a conventional hydraulic press (Metalmaster PP-10HD) at 20 MPa for 2 min; to avoid breaking the glass substrate, the cell and electrode were sandwiched between ≈ 1.5 mm thick rubber (Translucent silicon rubber RS Component Pty Ltd). Gold electrodes were produced by evaporating a 80 nm thick Au layer (DDHightech GCMO3CR; initial vacuum level 8×10^{-6} Torr) over the HTM layer with a constant rotation of the stage; customized metal photomask was applied to produce solar cells with an active area of 0.16 cm^2.

Characterization: All samples used for characterization were deposited by the optimized hot-casting assisted spin-coating method on TiO_2 or glass supports as relevant.

X-ray diffraction (XRD) patterns were obtained using a D2 Phaser BRUKER diffractometer with a Cu-K_α radiation (λ = 1.5406 Å) source operating at 30 kV and 15 mA at a scan rate of 0.5° min^{-1}. For the analysis, freshly produced films with a thickness of 200 nm on glass slides were employed. Vesta software was used to generate crystal structures displayed in Figure 2b.

X-ray photoelectron spectroscopic (XPS) analysis was performed with a Nexsa Surface Analysis System (Thermo Fisher Scientific) on the 200 nm thick copper silver bismuth iodide films spin-coated onto 2.5 cm × 2.5 cm c-TiO_2|FTO substrates. Analysis was undertaken with a monochromated Al K_α X-rays (1486.6 eV) source at a power of 72 W (12 kV × 6 mA) and a hemispherical analyzer operating in a fixed analyzer transmission mode. During analysis, the base pressure was typically less than 5.0×10^{-9} mbar. Survey and high-resolution scans were recorded at analyzer pass energies of 150 and 50 eV, respectively. Survey scans were performed with a step size of 1.0 eV and a dwell time of 10 ms. High-resolution spectra were recorded with 0.1 eV step size and dwell time of 50 ms, typically yielding a full width at half of the maximum of 0.8–0.9 eV for the Ag $3d^{5/2}$ peak for the performance tests. A low-energy dual-beam (ion and electron) flood gun was used to compensate for surface charging. Samples were analyzed at a nominal photoelectron emission angle of 0°.

Data processing was performed using Thermoscientific Avantage processing software version 5.9925. All elements present were identified from survey spectra. The atomic concentrations of the detected elements were calculated using integral peak intensities and the sensitivity factors supplied by the manufacturer. Binding energies were corrected to the C 1s peak at 284.8 eV (aliphatic hydrocarbon). The accuracy associated with quantitative XPS is ≈ 10–15%. Precision, i.e., reproducibility, depends on the signal: noise ratio and is usually better than 5%.

Scanning electron micrographs (SEM) were collected using a FEI Magellan 400 XHR FEGSEM at a voltage of 3–5 kV and spot size 2. Freshly deposited Cu_xAgBiI_{4+x} + m-TiO_2|c-TiO_2|FTO samples were immobilized on a specimen stub using double-sided carbon tape, and the copper tape was employed to create electrical contact for top-view imaging. For side-view imaging, complete Ag|HTM|Cu_xAgBiI_{4+x} + m-TiO_2|c-TiO_2|FTO devices were cracked using a glass cutter and pliers, and samples were immobilized in a TED PELLA, Inc. cross-sectional side-view holder and coated with iridium to avoid charging. A Bruker Quantax silicon drift detector was used to record energy dispersive X-ray spectra at a voltage of 10 kV and a spot size of 4.5.

Inductively coupled plasma optical emissions spectroscopic (ICP-OES) analysis was undertaken using a Perkin Elmer's Avio 200 ICP instrument. Calibration samples were made by diluting a multi-element commercial standard solution (Sigma Aldrich). Characterization samples were prepared by immersing the Cu_xAgBiI_{4+x} films deposited onto the glass in 1 mL of 2 wt% HNO_3 aqueous solution overnight, which resulted in complete dissolution of the materials of interest.

Thermogravimetric analysis (TGA) was conducted using a Mettler Toledo Thermogravimetric Analyzer 2 Star System. Nitrogen gas was used during the analysis at a 20 mL min^{-1} rate with a temperature ramp rate of 10 °C min^{-1} from 25 to 500 °C. Samples were heated in 40 µL alumina crucibles.

UV–vis spectra were recorded for the freshly-prepared Cu_xAgBiI_{4+x} + m-TiO_2|c-TiO_2|FTO samples in transmission and reflectance modes using a Perkin Elmer Lambda 1050 spectrophotometer equipped with an integrating sphere. UV-vis spectra of the m-TiO_2|c-TiO_2|FTO substrates were used to correct the absorption data. The absorption coefficients were calculated using the equation reported in the literature, using the film thickness derived from the SEM cross-section images.[29]

Photoluminescence measurements demonstrated in Figure 4 and Figure S13 (Supporting Information) were carried out using an Edinburgh Instruments Ltd. FLSP920 time-correlated single-photon counting (TCSPC) spectrometer with a 465.8 nm pulsed diode laser excitation source (EPL-475, Edinburgh Instruments Ltd.) having a pulse width of ≈100 ps and a peak fluence of ≈0.2 nJ cm^{-2} (2 W cm^2). Decay curves and spectra were measured using a pulse repetition rate of 50 kHz and 1 MHz, respectively. Luminescence was detected via a grating monochromator and photomultiplier tube. Emission spectra were corrected for the wavelength response of the detection system. Excitation and luminescence detection of samples were from the coated side of samples consisting of spin-coated films on 25 mm × 25 mm glass substrates.

Steady-state photoluminescence measurements displayed in Figures S14 and S15 (Supporting Information) were carried out using a Kymera 328i spectrometer with a Zylar 4.2 PLUS sCMOS and 150 lines mm^{-1} grating for samples mounted in a Nikon Ti2 microscope base with a 130 W mercury lamp. The light was monochromated using a Semrock bright line filter cube to provide either 405 or 488 nm excitation. Where relevant, spectra intensities were corrected using published efficiency losses for the various optics within the microscope and spectrometer. Samples were exposed to air for 2–4 min before measuring the PL intensity at specific intervals.

Photoelectron spectroscopy in air (PESA) measurements were accomplished using a Riken Kekei AC-2 spectrometer with a power intensity range of 20 to 50 nW. Cu_xAgBiI_{4+x} films of 200 nm thickness were deposited onto 2.5 cm × 2.5 cm c-TiO_2|FTO substrates for analysis.

Electron beam-induced current/scanning electron microscopy (EBIC/SEM) experiments were performed in a FEI Nova NanoSEM FEG-SEM equipped with a Deben Type 31 SEM specimen current EBIC amplifier at a relatively low accelerating voltage of 2 kV and beam currents of 30–50 pA without external bias to achieve a high-resolution probe with a decent signal-to-noise ratio while preserving low injection EBIC conditions.[40] Surface recombination can occur due to sample preparation and attachment damage, limiting EBIC observations. As a result, cross-section samples were prepared using a high-precision glass cutter and connected by wrapping Kapton tape around the substrate except for the imaging region. When applied to carbon electrodes, these preparation procedures were ineffective, which urged us to undertake experiments with the gold electrode-based solar cells. Because the samples had to be physically placed on the EBIC stage, the measured device cross-sections for each sample preparation procedure were exposed to air for several minutes before loading into the SEM. In addition, because these materials were susceptible to electron beam exposure, each cross-section area could only be scanned once. As a result, the measured EBIC declined after each initial EBIC scan regardless of the sample. Line/area intensity gradient profile in arbitrary units proportional to electric current was generated from the obtained EBIC images using ImageJ software.

Photovoltaic Measurements: A system developed by Surmiak et al.[41] for high throughput characterization of solar cells was used in the present study. A small amount of solder was added to the device edges to connect the ports and the cell electrodes. The devices were lit by an Abet Technologies Sun 3000 class AAA solar simulator calibrated at AM 1.5 (100 mW cm^2) intensity through a 0.16 cm^2 aperture mask, and *J*–*V* data were recorded using a 16-channel Bio-Logic VMP3 electrochemical workstation. No specific pre-treatment or pre-conditioning procedures were applied, as solar cells did not change their performance while being stored under ambient conditions. Current density (*J*)–voltage (*V*) scans were recorded in both backward (0.8 to –0.1 V) and forward (–0.1 to 0.8 V) directions with 0.010 V steps and settling periods of 100 ms, *viz*. at nominal scan rate 0.200 V s^{-1}, except for the data in Figures S20 and S22 where a scan rate of 0.100 V s^{-1} was used. No significant differences in the data obtained at these two scan rates were observed. The devices were illuminated for 10 s before testing to stabilize them. The steady-state efficiency was calculated by measuring the photocurrent at a constant potential matching the highest power voltage in the reverse *J*–*V* scan.

The illumination light source was chopped at 8 Hz, and the electrical signal was collected by a lock-in amplifier (Merlin Radiometric Lock-In Amplifier, Newport) under short-circuit conditions. A calibrated silicon diode (70356-70316NS, Newport) with a known spectral response spectrum was used as a reference.

The incident photon to current conversion efficiency (IPCE) spectra were measured with a Keithley 2400 Source Meter and an Oriel Cornerstone 260¼ m monochromator under 300 W Newport xenon lamp illumination. A calibrated silicon cell (Peccell Technologies) with known spectral response spectra was used to measure the monochromatic photon flow.

A Zahner Zennium electrochemical workstation with a frequency response analyzer module was used to acquire impedance spectroscopic data. A sinusoidal potential perturbation with an amplitude of 0.010 V was used to make measurements throughout a frequency range of 2 MHz to 0.1 Hz. Solar cells were illuminated using a white light-emitting diode during measurements. The output intensity was calibrated to generate the same photocurrent obtained using the Abet Technologies Sun 3000 class AAA source under 1 sun irradiation. The impedance data were modelled using the Z-View software.

Supporting Information

Supporting Information is available from the Wiley Online Library or from the author.

Acknowledgements

The authors are highly grateful to Dr. Jiangfeng Lu (Wuhan University of Technology) for invaluable discussions, Mr. Philippe Holzhey (Oxford University) for assistance with PL measurements, Mr. D. Vowles (Monash University) for assistance with EBIC experiments, and to the Monash Centre for Electron Microscopy and Monash X-ray Platform for providing access to their characterization facilities used for some parts of this work. The authors acknowledge funding of this work by the Australian Government through the Australian Centre for Advanced Photovoltaics (ACAP), the Australian Renewable Energy Agency (ARENA), and the Australian Research Council through the Centre of Excellence in Exciton Science (CE170100026) and Future Fellowship to ANS (FT200100317). Responsibility for the views, information, or advice expressed herein is not accepted by the Australian Government. SRR acknowledges the support from "laCaixa" Foundation (ID 100010434; LCF/BQ/PI20/11760024).

Open access publishing facilitated by Monash University, as part of the Wiley – Monash University agreement via the Council of Australian University Librarians.

Conflict of Interest

The authors declare no conflict of interest.

Data Availability Statement

The data that support the findings of this study are available from the corresponding author upon reasonable request.

Keywords

$CuAgBiI_5$, Cu_2AgBiI_6, solar cells, thin film

Received: April 30, 2022
Revised: June 1, 2022
Published online: July 17, 2022

[1] a) A. K. Jena, A. Kulkarni, T. Miyasaka, *Chem. Rev.* **2019**, *119*, 3036; b) N.-G. Park, M. Grätzel, T. Miyasaka, K. Zhu, K. Emery, *Nat. Energy* **2016**, *1*, 16152; c) N. G. Park, K. Zhu, *Nat. Rev. Mater.* **2020**, *5*, 333.

[2] a) F. Igbari, Z. K. Wang, L. S. Liao, *Adv. Energy Mater.* **2019**, *9*, 1803150; b) Z. Xiao, Z. Song, Y. Yan, *Adv. Mater.* **2019**, *31*, 1803792; c) W. Ke, M. G. Kanatzidis, *Nat. Commun.* **2019**, *10*, 965; d) N. Glück, T. Bein, *Energy Environ. Sci.* **2020**, *13*, 4691.

[3] a) G. Volonakis, M. R. Filip, A. A. Haghighirad, N. Sakai, B. Wenger, H. J. Snaith, F. Giustino, *J. Phys. Chem. Lett.* **2016**, *7*, 1254; b) M. Wang, W. Wang, B. Ma, W. Shen, L. Liu, K. Cao, S. Chen, W. Huang, *Nano-Micro Lett.* **2021**, *13*, 62.

[4] a) L. Zhang, K. Wang, B. Zou, *ChemSusChem* **2019**, *12*, 1612; b) N. C. Miller, M. Bernechea, *APL Mater.* **2018**, *6*, 084503; c) F. Ünlü, M. Deo, S. Mathur, T. Kirchartz, A. Kulkarni, *J. Phys. D: Appl. Phys.* **2022**, *55*, 113002; d) N. Tewari, S. B. Shivarudraiah, J. E. Halpert, *Nano Lett.* **2021**, *21*, 5578; e) S. Attique, N. Ali, S. Ali, R. Khatoon, N. Li, A. Khesro, S. Rauf, S. Yang, H. Wu, *Adv. Sci.* **2020**, *7*, 1903143; f) R. L. Z. Hoye, J. Hidalgo, R. A. Jagt, J.-P. Correa-Baena, T. Fix, J. L. MacManus-Driscoll, *Adv. Energy Mater.* **2022**, *12*, 2100499.

[5] a) Y. Kim, Z. Yang, A. Jain, O. Voznyy, G. H. Kim, M. Liu, L. N. Quan, F. P. García de Arquer, R. Comin, J. Z. Fan, E. H. Sargent, *Angew. Chem., Int. Ed.* **2016**, *55*, 9586; b) I. Turkevych, S. Kazaoui, E. Ito, T. Urano, K. Yamada, H. Tomiyasu, H. Yamagishi, M. Kondo, S. Aramaki, *ChemSusChem* **2017**, *10*, 3754; c) V. Pecunia, J. Zhao, C. Kim, B. R. Tuttle, J. Mei, F. Li, Y. Peng, T. N. Huq, R. L. Z. Hoye, N. D. Kelly, S. E. Dutton, K. Xia, J. L. MacManus-Driscoll, H. Sirringhaus, *Adv. Energy Mater.* **2021**, *11*, 2003968.

[6] a) N. Pai, J. Lu, T. R. Gengenbach, A. Seeber, A. S. R. Chesman, L. Jiang, D. C. Senevirathna, P. C. Andrews, U. Bach, Y.-B. Cheng, A. N. Simonov, *Adv. Energy Mater.* **2019**, *9*, 1803396; b) Z. Hu, Z. Wang, G. Kapil, T. Ma, S. Iikubo, T. Minemoto, K. Yoshino, T. Toyoda, Q. Shen, S. Hayase, *ChemSusChem* **2018**, *11*, 2930; c) K. W. Jung, M. R. Sohn, H. M. Lee, I. S. Yang, S. D. Sung, J. Kim, E. Wei-Guang Diau, W. I. Lee, *Sustainable Energy Fuels* **2018**, *2*, 294; d) W.-X. Chai, L.-M. Wu, J.-Q. Li, L. Chen, *Inorg. Chem.* **2007**, *46*, 1042.

[7] A. Kulkarni, F. Ünlü, N. Pant, J. Kaur, C. Bohr, A. K. Jena, S. Öz, M. Yanagida, Y. Shirai, M. Ikegami, K. Miyano, Y. Tachibana, S. Chakraborty, S. Mathur, T. Miyasaka, *Sol. RRL* **2021**, *5*, 2100077.

[8] a) B. Zhang, Y. Lei, R. Qi, H. Yu, X. Yang, T. Cai, Z. Zheng, *Sci. China Mater.* **2019**, *62*, 519; b) L. Wang, Y. Bao, S. Wang, F. Wang, C. Xie, K. T. Butler, X. Fan, *Cryst. Growth Des.* **2021**, *21*, 2850; c) N. Qu, Y. Lei, X. Yang, X. Hu, W. Zhao, C. Zhao, Z. Zheng, *J. Mater. Chem. C* **2020**, *8*, 8451.

[9] a) C. N. Savory, A. Walsh, D. O. Scanlon, *ACS Energy Lett.* **2016**, *1*, 949; b) Y. Cai, W. Xie, Y. T. Teng, P. C. Harikesh, B. Ghosh, P. Huck, K. A. Persson, N. Mathews, S. G. Mhaisalkar, M. Sherburne, M. Asta, *Chem. Mater.* **2019**, *31*, 5392.

[10] a) A. H. Slavney, T. Hu, A. M. Lindenberg, H. I. Karunadasa, *J. Am. Chem. Soc.* **2016**, *138*, 2138; b) M. Delor, A. H. Slavney, N. R. Wolf, M. R. Filip, J. B. Neaton, H. I. Karunadasa, N. S. Ginsberg, *ACS Energy Lett.* **2020**, *5*, 1337; c) D. Bartesaghi, A. H. Slavney, M. C. Gelvez-Rueda, B. A. Connor, F. C. Grozema, H. I. Karunadasa, T. J. Savenije, *J. Phys. Chem. C* **2018**, *122*, 4809; d) E. T. McClure, M. R. Ball, W. Windl, P. M. Woodward, *Chem. Mater.* **2016**, *28*, 1348.

[11] a) Z. Li, S. P. Senanayak, L. Dai, G. Kusch, R. Shivanna, Y. Zhang, D. Pradhan, J. Ye, Y.-t. Huang, H. Sirringhaus, R. A. Oliver, N. C. Greenham, R. H. Friend, R. L. Z. Hoye, *Adv. Funct. Mater.* **2021**, *31*, 2104981; b) J. Leveillee, G. Volonakis, F. Giustino, *J. Phys. Chem. Lett.* **2021**, *12*, 4474; c) H. Lei, D. Hardy, F. Gao, *Adv. Funct. Mater.* **2021**, *31*, 2105898.

[12] G. Longo, S. Mahesh, L. R. V. Buizza, A. D. Wright, A. J. Ramadan, M. Abdi-Jalebi, P. K. Nayak, L. M. Herz, H. J. Snaith, *ACS Energy Lett.* **2020**, *5*, 2200.

[13] a) F. Igbari, R. Wang, Z.-K. Wang, X.-J. Ma, Q. Wang, K.-L. Wang, Y. Zhang, L.-S. Liao, Y. Yang, *Nano Lett.* **2019**, *19*, 2066; b) R. L. Z. Hoye, L. Eyre, F. Wei, F. Brivio, A. Sadhanala, S. Sun, W. Li, K. H. L. Zhang, J. L. MacManus-Driscoll, P. D. Bristowe, R. H. Friend, A. K. Cheetham, F. Deschler, *Adv. Mater. Interfaces* **2018**, *5*, 1800464; c) W. Gao, C. Ran, J. Xi, B. Jiao, W. Zhang, M. Wu, X. Hou, Z. Wu, *ChemPhysChem* **2018**, *19*, 1696; d) E. Greul, M. L. Petrus, A. Binek, P. Docampo, T. Bein, *J. Mater. Chem. A* **2017**, *5*, 19972.

[14] Q. Li, Y. Wang, W. Pan, W. Yang, B. Zou, J. Tang, Z. Quan, *Angew. Chem., Int. Ed.* **2017**, *56*, 15969.

[15] K. z. Du, W. Meng, X. Wang, Y. Yan, D. B. Mitzi, *Angew. Chem., Int. Ed.* **2017**, *56*, 8158.

[16] a) N. Pai, J. Lu, M. Wang, A. S. R. Chesman, A. Seeber, P. V. Cherepanov, D. C. Senevirathna, T. R. Gengenbach, N. V. Medhekar, P. C. Andrews, U. Bach, A. N. Simonov, *J. Mater. Chem. A* **2020**, *8*, 2008; b) M. Keshavarz, E. Debroye, M. Ottesen, C. Martin, H. Zhang, E. Fron, R. Küchler, J. A. Steele, M. Bremholm, J. Van de Vondel, H. I. Wang, M. Bonn, M. B. J. Roeffaers, S. Wiedmann, J. Hofkens, *Adv. Mater.* **2020**, *32*, 2001878; c) J. Li, J. Duan, J. Du, X. Yang, Y. Wang, P. Yang, Y. Duan, Q. Tang, *ACS Appl. Mater. Interfaces* **2020**, *12*, 47408; d) H. Lei, D. Hardy, F. Gao, *Adv. Funct. Mater.* **2021**, *31*, 2105898.

[17] R. Nie, R. R. Sumukam, S. H. Reddy, M. Banavoth, S. I. Seok, *Energy Environ. Sci.* **2020**, *13*, 2363.

[18] X.-G. Zhao, J.-H. Yang, Y. Fu, D. Yang, Q. Xu, L. Yu, S.-H. Wei, L. Zhang, *J. Am. Chem. Soc.* **2017**, *139*, 2630.

[19] a) Z. Xiao, W. Meng, J. Wang, Y. Yan, *ChemSusChem* **2016**, *9*, 2628; b) N. Zarabinia, R. Rasuli, *Energy Sources, Part A* **2021**, *43*, 2443.

[20] P. Vishnoi, R. Seshadri, A. K. Cheetham, *J. Phys. Chem. C* **2021**, *21*, 11756.

[21] S. E. Creutz, E. N. Crites, M. C. De Siena, D. R. Gamelin, *Nano Lett.* **2018**, *18*, 1118.

[22] M. Li, F. Li, J. Gong, T. Zhang, F. Gao, W.-H. Zhang, M. Liu, *Small Struct.* **2022**, *3*, 2100102.

[23] H. C. Sansom, G. Longo, A. D. Wright, L. R. V. Buizza, S. Mahesh, B. Wenger, M. Zanella, M. Abdi-Jalebi, M. J. Pitcher, M. S. Dyer, T. D. Manning, R. H. Friend, L. M. Herz, H. J. Snaith, J. B. Claridge, M. J. Rosseinsky, Sansom, et al., *J. Am. Chem. Soc.* **2021**, *143*, 3983.

[24] H. C. Sansom, L. R. V. Buizza, M. Zanella, J. T. Gibbon, M. J. Pitcher, M. S. Dyer, T. D. Manning, V. R. Dhanak, L. M. Herz, H. J. Snaith, J. B. Claridge, M. J. Rosseinsky, *Inorg. Chem.* **2021**, *60*, 18154.

[25] A. Mutlu, C. Zafer, *Sol. Energy* **2022**, *234*, 190.

[26] D. Marongiu, M. Saba, F. Quochi, A. Mura, G. Bongiovanni, *J. Mater. Chem. C* **2019**, *7*, 12006.

[27] F. Zhang, Z. Hu, B. Zhang, Z. Lin, J. Zhang, J. Chang, Y. Hao, *ACS Appl. Mater. Interfaces* **2022**, *14*, 18498.

[28] T. C. T. Pham, H. S. Kim, K. B. Yoon, *Science* **2011**, *334*, 1533.

[29] N. Pai, J. Lu, D. C. Senevirathna, A. S. R. Chesman, T. Gengenbach, M. Chatti, U. Bach, P. C. Andrews, L. Spiccia, Y.-B. Cheng, A. N. Simonov, *J. Mater. Chem. C* **2018**, *6*, 2483.

[30] B. Tan, S. R. Raga, A. S. R. Chesman, S. O. Fürer, F. Zheng, D. P. McMeekin, L. Jiang, W. Mao, X. Lin, X. Wen, J. Lu, Y.-B. Cheng, U. Bach, *Adv. Energy Mater.* **2019**, *9*, 1901519.

[31] M. Bernechea, N. C. Miller, G. Xercavins, D. So, A. Stavrinadis, G. Konstantatos, *Nat. Photonics* **2016**, *10*, 521.

[32] M. K. Kashif, I. Benesperi, R. A. Milhuisen, S. Meyer, J. Hellerstedt, D. Zee, N. W. Duffy, B. Halstead, M. S. Fuhrer, J. Cashion, Y.-B. Cheng, L. Spiccia, A. N. Simonov, U. Bach, *ACS Energy Lett.* **2017**, *2*, 1855.

[33] G. A. Sepalage, H. Weerasinghe, N. Rai, N. W. Duffy, S. R. Raga, Y. Hora, M. Gao, D. Vak, A. S. R. Chesman, U. Bach, A. N. Simonov, *Adv. Mater. Technol.* **2021**, *7*, 2101148.

[34] a) Z. Zhang, X. Li, X. Xia, Z. Wang, Z. Huang, B. Lei, Y. Gao, *J. Phys. Chem. Lett.* **2017**, *8*, 4300; b) S. M. Jain, D. Phuyal, M. L. Davies, M. Li, B. Philippe, C. De Castro, Z. Qiu, J. Kim, T. Watson, W. C. Tsoi, O. Karis, H. Rensmo, G. Boschloo, T. Edvinsson, J. R. Durrant, *Nano Energy* **2018**, *49*, 614; c) Q. Zhang, C. Wu, X. Qi, F. Lv, Z. Zhang, Y. Liu, S. Wang, B. Qu, Z. Chen, L. Xiao, *ACS Appl. Energy Mater.* **2019**, *2*, 3651; d) F. Wei, Z. Deng, S. Sun, N. T. P. Hartono, H. L. Seng, T. Buonassisi, P. D. Bristowe, A. K. Cheetham, *Chem. Commun.* **2019**, *55*, 3721.

[35] a) B. Wang, N. Li, L. Yang, C. Dall'Agnese, A. K. Jena, T. Miyasaka, X.-F. Wang, *J. Am. Chem. Soc.* **2021**, *143*, 14877; b) B. Wang, N. Li, L. Yang, C. Dall'Agnese, A. K. Jena, S.-i. Sasaki, T. Miyasaka, H. Tamiaki, X.-F. Wang, *J. Am. Chem. Soc.* **2021**, *143*, 2207.

[36] a) N. E. Courtier, *Phys. Rev. Appl.* **2020**, *14*, 24031; b) T. Kirchartz, B. E. Pieters, J. Kirkpatrick, U. Rau, J. Nelson, *Phys. Rev. B* **2011**, *83*, 115209.

[37] E. von Hauff, D. Klotz, *J. Mater. Chem. C* **2022**, *10*, 742.

[38] a) J. Diekmann, P. Caprioglio, M. H. Futscher, V. M. Le Corre, S. Reichert, F. Jaiser, M. Arvind, L. P. Toro, E. Gutierrez-Partida, F. Peña-Camargo, C. Deibel, B. Ehrler, T. Unold, T. Kirchartz, D. Neher, M. Stolterfoht, *Sol. RRL* **2021**, *5*, 2100219; b) W. Shockley, H. J. Queisser, *J. Appl. Phys.* **1961**, *32*, 510.

[39] a) Y. Zhang, Y. Zhu, M. Hu, N. Pai, T. Qin, Y.-B. Cheng, U. Bach, A. N. Simonov, J. Lu, *J. Phys. Chem. Lett.* **2022**, *13*, 2792; b) Y. Cho, J. Bing, H. D. Kim, Y. Li, J. Zheng, S. Tang, M. A. Green, A. Wakamiya, S. Huang, H. Ohkita, A. W. Y. Ho-Baillie, *ACS Appl. Mater. Interfaces* **2021**, *13*, 39178.

[40] Barange, V. B. Chu, M. Nam, I.-H. Ahn, Y. D. Kim, I. K. Han, B. K. Min, D.-H. Ko, *Adv. Energy Mater.* **2016**, *6*, 1601114.

[41] M. A. Surmiak, T. Zhang, J. Lu, K. J. Rietwyk, S. R. Raga, D. P. McMeekin, U. Bach, *Sol. RRL* **2020**, *4*, 2000097.